

# Progress in Ternary Metal Oxides as Photocathodes for Water Splitting Cells: Optimization Strategies

María Isabel Díez-García\* and Roberto Gómez\*

The conversion of solar energy into fuels and, specifically hydrogen, is a critical process for ensuring the sustainability of the future energy system. Among the different ways of converting solar energy into fuels and chemicals, photoelectrochemical tandem cells, containing two photoactive materials, stand out as they have the potential for direct solar-to-fuel conversion, thus minimizing cost. The implementation of photoelectrolysis for hydrogen generation is hindered by the lack of suitable electrode materials, particularly photocathodes. Among the candidates for photocathodes, ternary (and multinary) transition metal oxides have the advantage of lower cost and, potentially, higher stability than other metal compounds. Herein, the aim is to provide an overview of the current state of the art for ternary oxides (spinel, delafossites, perovskites, etc.), with a focus on the modification strategies that can optimize their behavior and applicability. Both copper-based and iron-based ternary oxides are the most studied and, currently, the most promising. Among the strategies being used for their optimization, doping, the deposition of underlayers and overlayers, and the use of cocatalysts are the most popular. However, it is apparent that both solar-to-hydrogen efficiencies and stability will need to be addressed in the future. Some guidelines in this respect are also provided.

concern. Furthermore, the problem of the greenhouse effect has reached enormous proportions because of the global climate change experienced by the planet. This effect is mainly attributed to CO<sub>2</sub> emissions, although other gases, such as CH<sub>4</sub> or N<sub>2</sub>O also contribute to a minor extent.

The access to clean, carbon-free energy technologies that could compete with the price of fossil fuels, is expected to be a key factor for sustaining the future energy demand. Among them, nuclear power is an alternative that currently provides a considerable percentage of the electricity in Europe and the USA, but it has some associated problems such as the accumulation of radioactive fission products. Biomass is an attractive renewable source of energy as chemical energy is stored from the sun through photosynthesis but has the drawback of the large extensions of land required to produce the biomass fuels. In this regard, solar energy constitutes the sustainable source with the highest potential


to meet most of the energy needs.<sup>[1]</sup> The sun provides about 120 000 terawatts (TW) of power to the Earth, and exploiting only a fraction of the solar energy absorbed by the atmosphere, the land, and the oceans could potentially be a renewable solution to the current global energy challenge. It has been estimated that a land coverage of 0.16% with 10% efficient solar conversion systems would provide 20 TW of power.<sup>[2]</sup> The most efficient photovoltaic cells have very high efficiencies (more than 40%) on a laboratory scale.<sup>[3]</sup> Most of the commercial solar panels are based on Si, reaching power conversion efficiencies of 16%–21%.<sup>[4]</sup> Although the panel costs have been reduced in the last years, the technology is still too expensive to compete with fossil fuel systems.

The large-scale implementation of photovoltaic power plants would require grid-based storage capacities because of the intermittent nature of solar power. An interesting option is storing the solar electromagnetic energy into the chemical bonds contained in fuels such as H<sub>2</sub>, CH<sub>4</sub> or CH<sub>3</sub>OH. Particularly, the production of H<sub>2</sub> is attractive because it can be obtained from water, an abundant and cheap compound and, importantly, because their combustion is carbon-free, avoiding the problem of the greenhouse effect. In this context, photoelectrochemical (PEC) water splitting is a promising alternative, which consists in the conversion of water into H<sub>2</sub> and O<sub>2</sub> using semiconductor materials as photoelectrodes to convert sunlight energy into chemical energy

## 1. Introduction

Ensuring in a sustainable way the energy supply with the preservation of the current living standards of our society is one of the greatest challenges of the twenty-first century. The world energy consumption is expected to grow nearly 50% between 2020 and 2050. In 2019, fossil fuels provided about 80% of the total global energy supply, but this source cannot sustain the future energy demand for a long time because of finite reserves. The impact on both environment and human health derived from the use of fossil fuels is another serious

M. I. Díez-García, R. Gómez  
 Institut Universitari d'Electroquímica i Departament de Química Física  
 Universitat d'Alacant  
 E-03080 Alicante, Spain  
 E-mail: mariaisabel.diez@ua.es; roberto.gomez@ua.es

 The ORCID identification number(s) for the author(s) of this article can be found under <https://doi.org/10.1002/solr.202100871>.

© 2021 The Authors. Solar RRL published by Wiley-VCH GmbH. This is an open access article under the terms of the Creative Commons Attribution-NonCommercial-NoDerivs License, which permits use and distribution in any medium, provided the original work is properly cited, the use is non-commercial and no modifications or adaptations are made.

DOI: 10.1002/solr.202100871

(with or without the assistance of applied bias in the photoelectrochemical device). However, at present, 95% of the H<sub>2</sub> production results from steam reforming of CH<sub>4</sub> and other light hydrocarbons (from fossil fuels).<sup>[5]</sup> Market viability of the photoelectrochemical technology will depend on finding low-cost, long-lifetime, and highly efficient materials for energy conversion. This includes the development of strategies and materials that stabilize and improve the overall photoelectrochemical response.

Photoelectrochemical cells for water splitting can be designed with different configurations.<sup>[6–8]</sup> The simplest one consists of a single light absorber material. Specifically, a photoanode (photocathode) composed of an n-type (p-type) semiconductor, together with a metal (or other electrode material working in the dark) as a cathode (anode). When photons with energy higher than the bandgap are absorbed by the semiconductor, electron–hole pairs are photogenerated. They are spatially separated in the semiconductor by the presence of an electric field in the space charge region and/or through diffusion processes. The generated minority charge carriers, holes in n-type, and electrons in p-type semiconductors are driven to the semiconductor-liquid interface, inducing redox reactions. In the case of water splitting, electrons are employed to reduce water, producing H<sub>2</sub>, while holes are consumed in water oxidation, generating O<sub>2</sub>. The majority carriers are swept toward the back contact and transported to the counter electrode (commonly a metal) through the external circuit, supporting the other half-reaction (O<sub>2</sub> and H<sub>2</sub> evolution in cells based on p-type or n-type electrodes, respectively). When only one absorber material is employed (semiconductor), it must have adequate conduction and valence band edges for both half-reactions and absorb light with photon energies >1.23 eV to split water without applied bias under ideal kinetic conditions. However, the overpotentials needed for hydrogen and, especially, oxygen evolution increase the minimum required bandgap value well above 1.23 eV, even assuming that the band edges are precisely located to drive water splitting under minimum bandgap. Thus, the bandgap needed for photoelectrochemical water splitting using a single photoabsorber is reported to be around 2 eV at least,<sup>[8]</sup> which significantly diminishes the use of the solar spectrum. To deal with these drawbacks, a more practical, albeit simple, device for water photosplitting has been proposed, namely the tandem cell, which is composed of an adequate couple of photoabsorbers, a photocathode and a photoanode as depicted in **Figure 1**. Reported calculations have shown that a single absorber PEC system can reach a maximum solar-to-hydrogen (STH) efficiency of 31%, while tandem systems (with two absorbers) can reach a value of 40%.<sup>[9,10]</sup> Efficiencies above 15% can be attained by combining a semiconductor with a bandgap of 1–1.3 eV and another with a bandgap of 1.5–2.1 eV. In practice, finding an adequate couple of semiconductors having bandgaps comprised within these ranges is challenging.

Apart from the bandgap value constraint, which is crucial for achieving high STH efficiencies, the photoelectrodes should meet additional requirements. The most important ones for optimum operation are: (i) Adequate band edge locations for water reduction and oxidation reactions. (ii) High chemical stability in the dark and under illumination. (iii) Efficient charge transport (diffusion) across the semiconductor bulk. (iv) Low overpotentials for the water oxidation and reduction reactions. In addition,

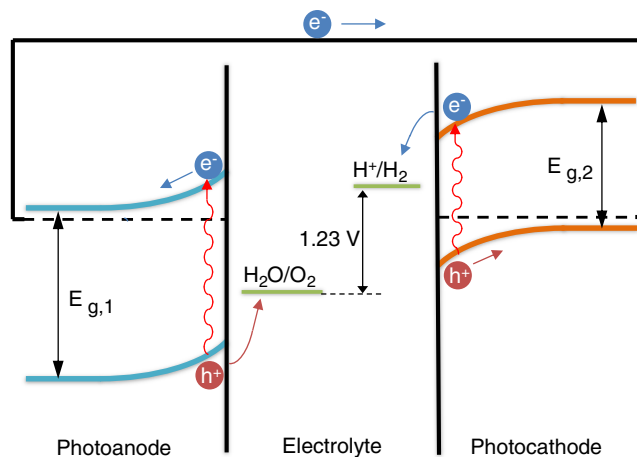


**Figure 1.** Idealized PEC tandem cell configuration under illumination schematizing the interfacial reactions for water splitting.

there are other requirements related to the viability of a practical device: (v) Low-cost reagents for electrode synthesis. (vi) Low-cost and scalable synthesis route. (vii) Materials composed of Earth abundant elements. (viii) Nontoxic and environmentally friendly materials.

Since the seminal work by Fujishima and Honda,<sup>[11]</sup> a large number of reports dealing with the study and optimization of n-type materials for photoelectrochemical cells have appeared in the literature. Up to now, TiO<sub>2</sub> has been considered as the reference n-type semiconductor material owing to its high photoactivity, nontoxicity, inertness, low cost, and abundance on Earth.<sup>[12–14]</sup> Unfortunately, it possesses a bandgap of 3–3.2 eV and it can only absorb photons in the UV range, which has motivated intense research on narrower bandgap materials such as hematite,<sup>[13,15–18]</sup> WO<sub>3</sub>,<sup>[19–21]</sup> and BiVO<sub>4</sub>.<sup>[22–26]</sup>

It is worth noting that the number of reports dealing with oxide photocathode materials is much scarcer than in the case of photoanodes mainly because, in general, p-type semiconductor metal oxides display poor corrosion resistance and, sometimes, low carrier mobility. Consequently, finding a high-efficiency, low-cost, and stable photocathode keeps on being a pending task. Earlier studies focused on nonoxide materials, such as group III-V materials (like InP<sup>[27–29]</sup>), Si<sup>[30–34]</sup> and SiC,<sup>[35–37]</sup> and chalcogenides.<sup>[38]</sup> Most of them have demonstrated high photoresponses although the stability is usually compromised as well as availability. In general, metal oxides present the advantage of simpler synthesis procedures and higher chemical stability. In this regard, some reports have dealt with the state-of-the-art of photocathodes for water splitting<sup>[3,8,38–44]</sup> and some of them specifically focused on metal oxides.<sup>[45–50]</sup> Among those composed of nontoxic and earth-abundant metals, copper oxides (CuO and Cu<sub>2</sub>O) have been extensively studied,<sup>[51–58]</sup> especially Cu<sub>2</sub>O. Despite the high photoresponses attained, the major bottleneck of this material (and also of CuO) for water photoreduction lies in its instability in aqueous solutions under illumination,<sup>[51,52,54]</sup> leading to a photocurrent decay linked to the reduction of Cu ions. In the last years, significant efforts have been devoted to address this limitation by using protective layers. Some strategies, such as the introduction of AZO(Al:ZnO)/TiO<sub>2</sub>

layers and the loading of a cocatalyst have led to significant improvements relating to both stability and efficiency.<sup>[54,59,60]</sup> Despite these efforts, a copper oxide photoelectrode for a commercially viable solar hydrogen device has not been accomplished yet.

For reaching the goal of viable high-efficiency tandem cells for hydrogen production, substantial work is still needed. Currently, the main limitations of these devices are related to the stability and the low efficiencies of the photoelectrodes. Unfortunately, many materials that exhibit suitable efficiencies under visible light are found to be quite unstable under illumination, especially in the case of photocathodes. The main efforts for alleviating the durability issue focus on (i) the implementation of protective surface coatings on materials already reported and (ii) finding new compounds that exhibit superior stabilities. Additionally, efficiencies must be improved by enhancing sunlight absorption and charge carrier separation and collection. Depending on the design of the tandem cell, the use of transparent substrates for the photocathode may be a requirement as a single light beam should impinge both electrodes. In any case, the cost of hydrogen production must be considered, and the use of cost-effective reagents and procedures favored.

The limited number of useful binary metal oxides in electrochemistry makes it difficult to find a material with adequate properties as a photocathode. More complex metal oxides (i.e., ternary, quaternary oxides) behave as semiconductors and present high stability in aqueous environments. Indeed, many of them have a suitable bandgap to absorb visible light and they have an appropriate conduction band (CB) edge position for water reduction.<sup>[45,46]</sup> This has motivated the release of a substantial number of works devoted to ternary metal oxides (TMOs) based on earth-abundant metals in the last years. The present review aims to provide an overview of the state of the art of ternary oxide photocathodes for water splitting, including the most employed strategies to deliver high efficiencies and stabilities.

## 2. Ternary Oxides as Photocathodes

In the search for potential candidates for photocathodes, one question that arises is how to select among the existing tens of thousands of TMOs, particularly when only a small group of materials has been studied. In this respect, three different

systematic approaches can be adopted to identify the best candidates for water splitting: (i) the combinatorial approach has been used by the group of Parkinson for identifying new complex oxide materials in the framework of the Solar Hydrogen Activity Research Kit (SHArK) project.<sup>[61–71]</sup> An inkjet printing of metal oxide precursors is used to fabricate multimetal oxides with different compositions on the same conductive glass plate. The sample is submitted to a thermal treatment. Then, the resulting film is immersed into an aqueous electrolyte and a laser scanner interrogates locally the multinary metal oxide thin film to detect photoelectrochemical activity under visible light. (ii) A second approach is based on a computational screening of materials. Density functional theory (DFT) calculations allow for the prediction of properties such as the bandgap, band edge locations, effective carrier masses and optical properties. (iii) A third approach would be merely bibliographic, and it would entail the selection of the materials based on the properties reported in different studies, not necessarily related to photoelectrochemical applications. The scheme in **Figure 2** illustrates the approximate band edge positions (and bandgaps) of different TMOs studied as photocathodes for water splitting. They have adequate bandgaps and CB edge positions for being used in water-splitting photoelectrochemical tandem cells under solar irradiation. Moreover, in many Fe-based materials, CuBi<sub>2</sub>O<sub>4</sub> and some tantalates, CB and VB edge positions straddle both the O<sub>2</sub> and H<sub>2</sub> redox couple levels, being potentially useful in single-photoabsorber PEC cells. In this section, the main investigations on ternary oxides as photocathodes for water splitting are reviewed. The information has been organized according to the crystalline structure of the oxides grouped in families. **Table 1** summarizes some relevant parameters for evaluating the PEC activity of TMOs for their application in tandem cells.

### 2.1. Spinel

Spinel are compounds with the general formula AB<sub>2</sub>O<sub>4</sub>, where A and B are metals with oxidation states +2 and +3, respectively. Normal spinels crystallize in a close-packed cubic structure, although the unit cell can also belong to the orthorhombic group. The structure of the mineral spinel MgAl<sub>2</sub>O<sub>4</sub> is represented in **Figure 3a** in which B<sup>3+</sup> cations occupy octahedral sites while A<sup>2+</sup> occupy tetrahedral ones. Inverse spinels, such as NiFe<sub>2</sub>O<sub>4</sub>,

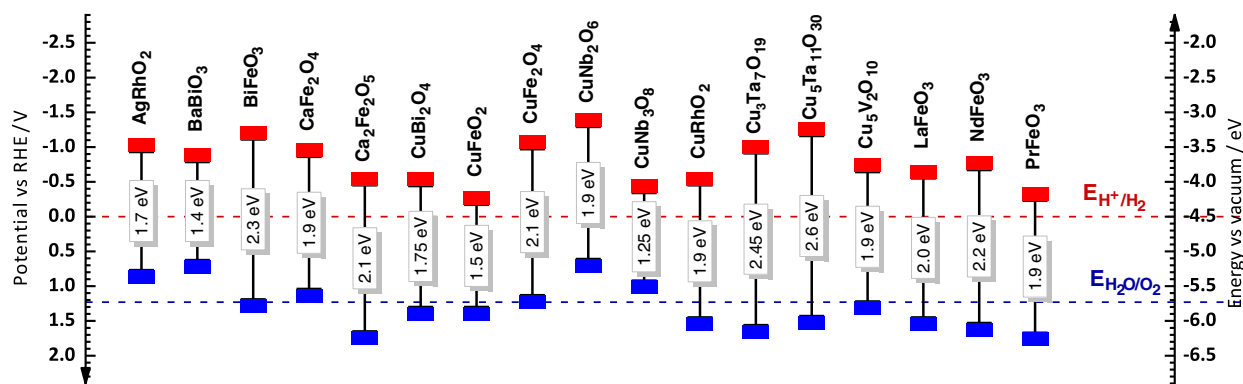


**Figure 2.** Band energy diagram showing the band edge positions (at pH = 0) with respect to the vacuum level and the reversible hydrogen electrode (RHE) for selected TMOs able to absorb in the visible and reported for PEC hydrogen production.

**Table 1.** Review of the main parameters for photoelectrochemical water reduction under 1 sun illumination for ternary metal oxide photocathodes: bandgap, photocurrent onset potential and IPCE (Dir. and Ind. stands for the bandgap values derived from Tauc plots for direct and indirect transitions, respectively).

Material	$E_g$ [eV]	$E_{onset}$ vs RHE [V]	IPCE [%] at 400 nm	Electrolyte	Ref.
BiFeO <sub>3</sub>	2.32 (Dir.)	0.75	0.21	0.1 M Na <sub>2</sub> SO <sub>4</sub>	[160]
	2.46 (Dir.) (ref. [157])	0.65 <sup>b),c)</sup>	0.15	0.1 M Na <sub>2</sub> SO <sub>4</sub>	[159]
	2.7 (Dir.)	0.87 <sup>b)</sup>	0.6 <sup>d)</sup>	0.1 M KOH	[204]
AgRhO <sub>2</sub>	1.7 eV	0.6 V (pH 0 to 7) 0.8 V (pH 9 to 14)	≈25	0.5 M KNO <sub>3</sub> adjusted to different pHs	[127]
CaFe <sub>2</sub> O <sub>4</sub>	1.9 (Ind.)	0.7–0.8	–	0.25 M K <sub>2</sub> SO <sub>4</sub> (pH 6), 0.1 M H <sub>2</sub> SO <sub>4</sub>	[77,78]
	1.9 <sup>a)</sup>	1.24 <sup>b)</sup>	≈3 <sup>d)</sup>	0.1 M NaOH, 0.1 M Na <sub>2</sub> SO <sub>4</sub> , 0.1 M H <sub>2</sub> SO <sub>4</sub>	[79]
	1.89 (Dir.)	1.0 <sup>b)</sup>	–	0.1 M Na <sub>2</sub> SO <sub>4</sub>	[80]
	1.85 (Dir.)	1.15	–	0.1 M Na <sub>2</sub> SO <sub>4</sub>	[81]
	1.9 (ref. [77])	≈0.9 <sup>c)</sup>	0.2 (at 408 nm)	0.1 M Na <sub>2</sub> SO <sub>4</sub>	[82]
Ca <sub>2</sub> Fe <sub>2</sub> O <sub>5</sub>	2.1 eV (Dir.)	1.22	–	0.5 M borate buffer (pH 11)	[171]
CuBi <sub>2</sub> O <sub>4</sub>	1.4–1.5 (Dir.)	1.05	≈1.1 <sup>d)</sup>	0.1 M Na <sub>2</sub> SO <sub>4</sub> adjusted pH 10.8	[91]
	1.8 <sup>a)</sup>	–	–	–	–
	1.8 (Dir.)	0.55 <sup>b)</sup>	≈3 (at 450 nm) <sup>d)</sup>	0.1 M Na <sub>2</sub> SO <sub>4</sub> (pH 6)	[233]
	1.8 <sup>a)</sup>	>1.0	≈2 <sup>d)</sup>	0.3 M K <sub>2</sub> SO <sub>4</sub> and 0.2 M phosphate buffer (pH 6.65)	[94]
	1.83 (Dir.)	1.1 <sup>c)</sup>	–	0.1 M NaOH (pH 12.8)	[93]
	1.6 eV (Ind.)	≈1	≈0.75 <sup>d)</sup>	0.1 M Na <sub>2</sub> SO <sub>4</sub>	[96]
	1.72 (Dir.)	≈1 <sup>c)</sup>	≈4	0.3 M K <sub>2</sub> SO <sub>4</sub> and 0.2 M phosphate buffer (pH 6.65)	[205]
	1.77 eV (Dir.)	>1	≈5 <sup>d)</sup>	0.132 M KOH + 0.05 M KCl (pH 13)	[100]
	1.82 (Dir.)	0.9	≈10 <sup>d)</sup>	0.1 M Na <sub>2</sub> SO <sub>4</sub> (pH 6.8)	[101]
	1.74 <sup>a)</sup>	1.15	≈10 <sup>d)</sup>	0.5 M NaOH (pH 13.5)	[108]
	1.5	≈1 <sup>c)</sup>	≈7 <sup>d)</sup>	0.3 M K <sub>2</sub> SO <sub>4</sub> and 0.2 M phosphate buffer (pH 6.65)	[207]
1.79 (Dir.)	1.2	≈13 <sup>d)</sup>	0.1 K <sub>2</sub> HPO <sub>4</sub> /K <sub>3</sub> PO <sub>4</sub> (pH = 11.66)	[104]	
CuCrO <sub>2</sub>	3.15 (Dir.)	1.06	≈1 <sup>d)</sup>	0.1 M HClO <sub>4</sub>	[129]
CuFeO <sub>2</sub>	≈1.55 <sup>a)</sup>	0.98	≈1.5 <sup>d)</sup>	1 M NaOH (pH 13.5)	[113]
	3.10 (Dir.)	0.9	–	1 M NaOH (pH 13.6)	[114]
	1.47 (Ind.)	–	–	–	–
–	0.8 <sup>c)</sup>	≈2 <sup>d)</sup>	1 M NaOH	[216]	
1.55 (Dir.)	0.65	–	1 M NaOH (pH 13.5)	[121]	
CuFe <sub>2</sub> O <sub>4</sub>	1.84 (Ind.)	1.05	≈16 <sup>d)</sup>	1 M NaOH (pH 13.5)	[217]
1.97–2.21 (Dir.)	0.89–1.07	6–18 (at 450 nm) <sup>d)</sup>	1 M H <sub>2</sub> SO <sub>4</sub>	[89]	
CuNbO <sub>3</sub>	≈2 <sup>a)</sup>	0.7 <sup>b)</sup>	≈3.5 <sup>d)</sup>	0.5 M Na <sub>2</sub> SO <sub>4</sub> (pH 6.3)	[136]
CuNb <sub>3</sub> O <sub>8</sub>	1.47 (Dir.)	0.7 <sup>b)</sup>	≈5.5 <sup>d)</sup>	0.5 M Na <sub>2</sub> SO <sub>4</sub> (pH 6.3)	[165]
1.26 (Ind.)	–	–	–	–	
CuRhO <sub>2</sub>	≈1.9 <sup>a)</sup>	1.0 <sup>b)</sup>	≈18 <sup>d)</sup>	1 M NaOH	[126]
Cu <sub>5</sub> Ta <sub>11</sub> O <sub>30</sub>	2.59 (Ref. [234]) <sup>a)</sup>	>0.7 <sup>b)</sup>	–	0.5 M Na <sub>2</sub> SO <sub>4</sub> (pH 6.3)	[163]
Cu <sub>3</sub> Ta <sub>7</sub> O <sub>19</sub>	2.47 (Ref. [234]) <sup>a)</sup>	>0.7 <sup>b)</sup>	≈3.5 <sup>d)</sup>	0.5 M Na <sub>2</sub> SO <sub>4</sub> (pH 6.3)	[163]
Cu <sub>3</sub> VO <sub>4</sub>	1.17 (Dir.)/1.14 (Ind.)	0.7 <sup>b),c)</sup>	–	0.5 M Na <sub>2</sub> SO <sub>4</sub> (pH 5.8)	[169]
LaFeO <sub>3</sub>	2.56 (Dir.)	1.1	≈0.35 <sup>d)</sup>	0.1 M Na <sub>2</sub> SO <sub>4</sub> adjusted pH to 12	[137]
	–	1.0 <sup>b),c)</sup>	≈1.8 <sup>d)</sup>	1 M NaOH	[138]
	2.0 (Ind.)	1.45	–	0.1 M NaOH	[139]
	2.7 (Dir.)	–	–	–	–
	2.16 (Dir.)	1.27	–	0.1 M NaOH (pH 13)	[144]
	2.4 (Dir.)	1.2	≈2.2 <sup>d)</sup>	0.1 M NaOH (pH 13)	[140]
	2.43 (Dir.)	1.3	–	0.1 M NaOH (pH 13.6)	[141]
LuRhO <sub>3</sub>	2.2	0.65 <sup>b),c)</sup>	–	Aqueous, adjusted to pH 7	[133,134]

**Table 1.** Continued.

Material	$E_g$ [eV]	$E_{\text{onset}}$ vs RHE [V]	IPCE [%] at 400 nm	Electrolyte	Ref.
$\text{Sr}_7\text{Fe}_{10}\text{O}_{22}$	1.8 (Ind.)	0.7 <sup>b)</sup>	–	0.25 M $\text{K}_2\text{SO}_4$ (pH 6)	[77]
$\text{YFeO}_3$	2.54 (Dir.)	1.15	<0.02	0.1 M NaOH	[146]
$\text{ZnRh}_2\text{O}_4$	2.0 (Ind.)	1.2	$\approx 8^{\text{d)}$	0.1 M $\text{Na}_2\text{SO}_4$ (pH 6)	[109]

<sup>a)</sup>value extrapolated from the absorption edge <sup>b)</sup>Calculated as  $E(V \text{ vs RHE}) = E(V \text{ vs ref}) + 0.059 \cdot \text{pH} + E_{\text{ref}}$ , where  $E_{\text{ref}}$  is the potential of the reference electrode with respect to SHE. When the measured pH value is not specified, the theoretically estimated value from the electrolyte composition is considered (except for 0.1 M  $\text{Na}_2\text{SO}_4$  for which pH = 6 is considered).  $E_{\text{ref}}(\text{SCE}) = 0.244 \text{ V}$  versus SHE and  $E_{\text{ref}}(\text{Ag}/\text{AgCl}(\text{sat.})) = 0.199 \text{ V}$  versus SHE<sup>[235]</sup> <sup>c)</sup>Read from a linear voltammogram under (chopped) illumination <sup>d)</sup>Read from an IPCE versus  $\lambda$  plot.

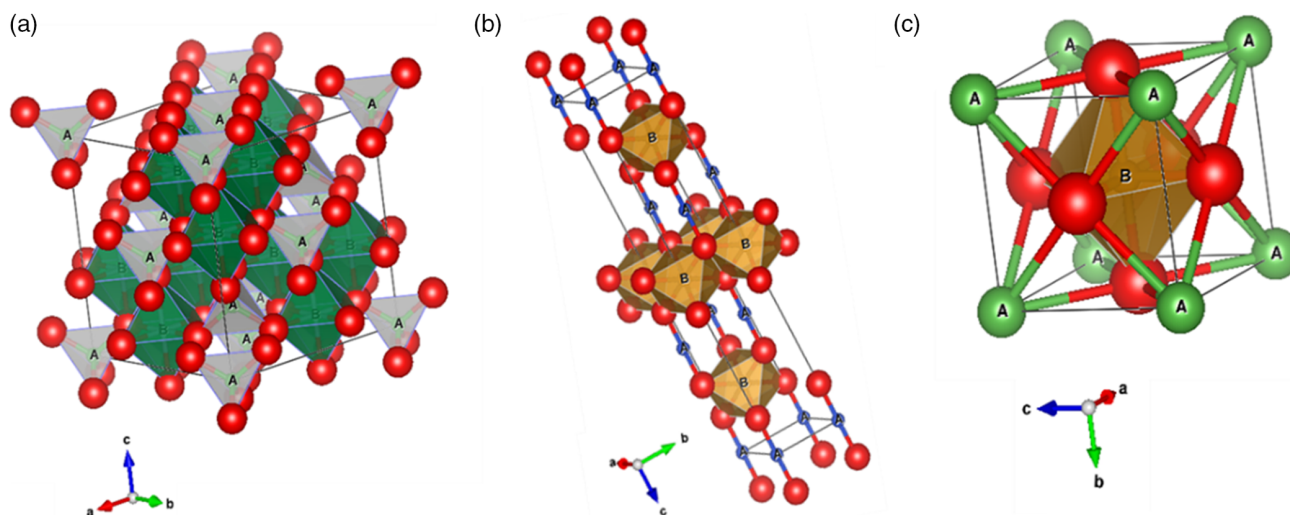


**Figure 3.** a)  $\text{MgAl}_2\text{O}_4$  cubic spinel ( $\text{AB}_2\text{O}_4$ ) (pattern 101-0129, COD database) with a space group Fd-3m. b)  $\text{CuFeO}_2$  ( $\text{ABO}_2$ ) delafossite structure (pattern 153-3117, COD database) with a space group R-3m (trigonal). c)  $\text{LaFeO}_3$  cubic perovskite ( $\text{ABO}_3$ ) (pattern 154-2144, COD database) with a space group Pm-3m.

have the same crystalline structure but the B cations occupy tetrahedral sites while half of the occupied octahedral sites are occupied by A and the other half by B.

Ferrites (B = Fe) constitute the most studied group of spinels in photocatalysis,<sup>[72]</sup> especially for water remediation. They are good candidates as PEC materials because they can exhibit both n-type and p-type behavior together with a relatively narrow bandgap, which enables them to absorb visible light.<sup>[73]</sup> In fact, their photocatalytic ability for H<sub>2</sub> production has already been studied.<sup>[72,74–76]</sup>

Calcium ferrite ( $\text{CaFe}_2\text{O}_4$ ) was one of the first ternary oxide materials studied as a photocathode for water splitting. Having a relatively narrow bandgap (1.9 eV), it can absorb visible light, and it has a suitable CB edge position for water reduction. Matsumoto et al.<sup>[77]</sup> were the first to describe the use of  $\text{CaFe}_2\text{O}_4$  as a photocathode for the hydrogen evolution reaction (HER) using a pellet sintered at high temperatures (1200 °C). They determined that Fermi level pinning (FLP) occurs at the semiconductor–electrolyte interface and consequently, low efficiencies were ascribed to a low electron concentration at the surface. Later, the same authors revealed that FLP arises from the presence of surface states linked to the redox levels of the  $\text{Fe}^{4+}/\text{Fe}^{3+}$  or  $\text{Fe}^{3+}/\text{Fe}^{2+}$  couples at the surface.<sup>[78]</sup>

Additionally, they managed to enhance the  $\text{CaFe}_2\text{O}_4$  photoresponse by improving the semiconductor/metal contact by sputtering an Au or Pt–Pd alloy film between the oxide and the Ag paste. Later, Ida et al.<sup>[79]</sup> constructed a tandem cell for water splitting in basic media using an (*hk*0)-oriented calcium ferrite film coated on a Pt substrate as a photocathode and a TiO<sub>2</sub> electrode as a photoanode (Figure 4a). Although H<sub>2</sub> and O<sub>2</sub> gases were detected (Figure 4b), the main drawback of  $\text{CaFe}_2\text{O}_4$  is the high temperature required for electrode preparation and the slow decomposition of the material because of photocorrosion reactions revealed by a decrease of the photocurrent over time (Figure 4c). Importantly, Cao and co-workers<sup>[80]</sup> were able to coat a fluorine-doped tin oxide (FTO) substrate with a 100 nm-thick  $\text{CaFe}_2\text{O}_4$  film by using PLD at relatively low temperatures for the first time. More recently, photoelectrochemical impedance spectroscopy (PEIS) was employed to investigate the kinetics and interfacial characteristics during photoelectrochemical hydrogen production in  $\text{CaFe}_2\text{O}_4$  photocathodes by developing an analytical interfacial model.<sup>[81]</sup> That work revealed that most of the photogenerated carriers recombine in the material bulk and that the interface is partly governed by FLP in agreement with the results reported by Matsumoto et al.<sup>[77,78]</sup> who uncovered that the presence of surface states precludes a substantial

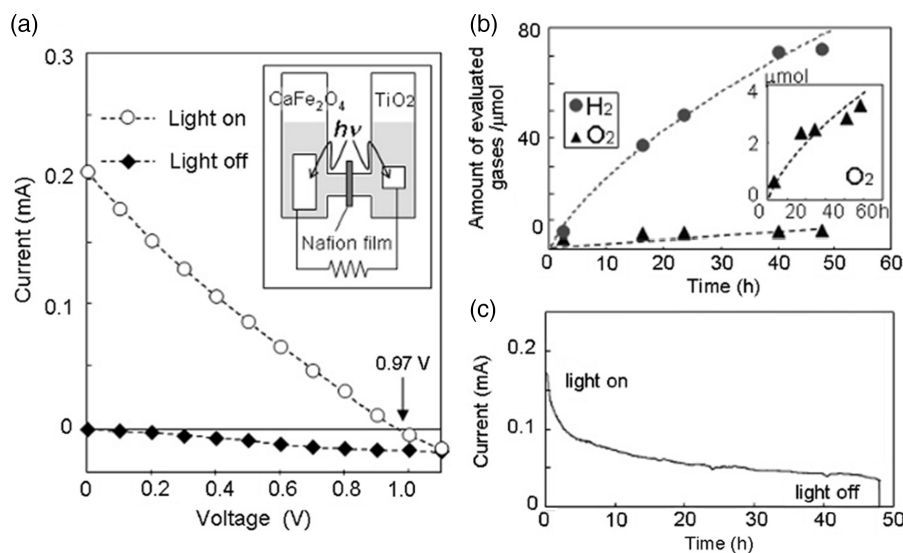


**Figure 4.** a) Current–potential curve for a photoelectrochemical cell, illustrated in the inset, composed of a  $\text{CaFe}_2\text{O}_4$  photocathode ( $2\text{ cm}^2$ ) and a  $\text{TiO}_2$  photoanode ( $0.5\text{ cm}^2$ ). b) Amount of photogenerated  $\text{H}_2$  and  $\text{O}_2$  and c) current–time curve of the photocell at short circuit. Reproduced with permission.<sup>[79]</sup> Copyright 2010, American Chemical Society.

increase of band bending with changes in the applied potential. More recently, Kirchberg et al.<sup>[82]</sup> obtained 250 nm-thick  $\text{CaFe}_2\text{O}_4$  films by using a simple sol-gel based synthesis, achieving hierarchical pore morphology by means of a polymer template. The charge separation efficiency calculated for these electrodes was very low, indicating a high bulk recombination rate, in agreement with the findings of Díez-García and Gómez.<sup>[81]</sup>

The spinels  $\text{CuFe}_2\text{O}_4$  and  $\text{ZnFe}_2\text{O}_4$  have been reported as photoanodes<sup>[83–86]</sup> or photocathodes<sup>[87,88]</sup> depending on the synthetic route. Díez-García et al. fabricated a  $\text{CuFe}_2\text{O}_4$ -based photocathode on a transparent substrate for the first time.<sup>[87]</sup> Despite the modest photocurrents detected, it stands out because of the adequate band position for  $\text{H}_2$  evolution, narrow bandgap, and the abundance of the constituent metals. More recently, Maitra et al.<sup>[89]</sup> synthesized nanoflake-like  $\text{CuFe}_2\text{O}_4$  through a two-step solvothermal method. First, hematite was solvothermally predeposited on conducting glass, with subsequent  $\text{Cu}^{2+}$  impregnation at different temperatures, which enabled controlling the degree of spinel inversion in the final ferrite material. Remarkably, IPCE values higher than 18% were achieved for wavelengths in the range of 450–500 nm.

Some  $\text{AB}_2\text{O}_4$  compounds not containing iron have also attracted considerable interest. For instance,  $\text{CuBi}_2\text{O}_4$  has also been widely investigated, especially in the last years,<sup>[90–108]</sup> since Arai et al. discovered its potential use as a new visible-light-responsive p-type semiconductor in 2007.<sup>[90]</sup> It crystallizes in a kusachiite-type structure consisting of  $\text{CuO}_4$  units staggered along the *c*-axis and separated by  $\text{Bi}^{3+}$  ions, each of which is linked to six O atoms (Figure 5a).<sup>[94]</sup> Hahn et al.<sup>[91]</sup> achieved the synthesis of photoactive  $\text{CuBi}_2\text{O}_4$  films composed of interconnected particles by electrodeposition. The material possesses a bandgap of 1.8 eV and a suitable photocurrent onset located at around 1.05 V versus RHE. Although the photocurrents were modest ( $25\text{--}35\ \mu\text{A cm}^{-2}$ ), they were stable (after an initial

decrease) for over 1 h of illumination at pH 10.8. However, the films were unstable in acidic electrolyte. The low photoconversion efficiency of these films was, in part, ascribed to hindered hole transport because of both a deficient particle attachment to the FTO (poor adhesion of the films) and the existence of interparticle boundaries. Later, a more profound analysis of  $\text{CuBi}_2\text{O}_4$  electrodes prepared by drop-casting was performed by Berglund et al.<sup>[94]</sup> Relevant properties for this material are summarized in the table of Figure 5a. That work revealed two different hole lifetimes of 32 ns and 819 ns, which implies that some of the photogenerated carriers recombine quickly while others are relatively long-lived. Furthermore, as the carrier diffusion length was much shorter (10 nm/52 nm) than the light penetration depth (244 nm for 550 nm light), most of the photogenerated carriers likely recombine before reaching the semiconductor/electrolyte interface. Apart from the poor hole transport, the formation of a Schottky barrier at the  $\text{CuBi}_2\text{O}_4/\text{FTO}$  interface is also a limiting factor for the photoelectrochemical performance. Finally, poor reaction kinetics for  $\text{H}_2$  evolution and/or the presence of electron traps at the surface are suggested to explain the dramatic increase of incident photon-to-current conversion efficiency (IPCE) values observed in the presence of  $\text{H}_2\text{O}_2$  as an electron scavenger (Figure 5b). The relatively narrow bandgap of  $\text{CuBi}_2\text{O}_4$ , together with the favorable photocurrent onset make this material promising for being coupled to wider bandgap n-type semiconductors in tandem cells. In fact, overall water splitting has been tested using  $\text{CuBi}_2\text{O}_4$  as a photocathode and  $\text{CuWO}_4$ ,<sup>[104]</sup>  $\text{ZnIn}_2\text{S}_4$ ,<sup>[105]</sup> or  $\text{W:BiVO}_4$ <sup>[103]</sup> as photoanodes. In some cases, the tandem cells have been shown to work under bias free conditions.

The photoelectrochemical properties of  $\text{ZnRh}_2\text{O}_4$  have recently been uncovered.<sup>[109]</sup> A porous photoelectrode was fabricated through electrophoresis using  $\text{ZnRh}_2\text{O}_4$  powder previously obtained through a solid state reaction. Having a bandgap of 2.0 eV and a very positive onset potential (1.2 V vs RHE), an

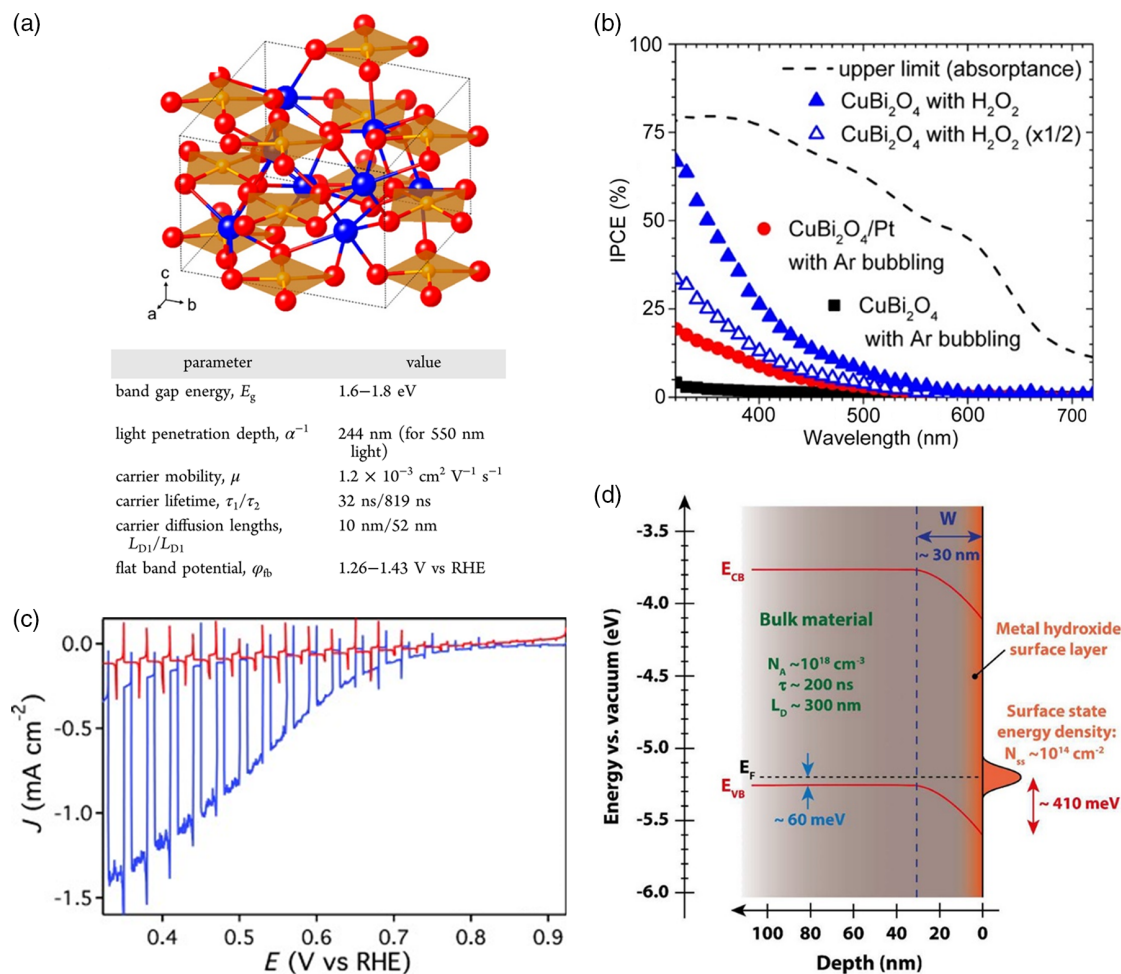


**Figure 5.** a) Crystal structure of  $\text{CuBi}_2\text{O}_4$ , being Bi, Cu, and O atoms the blue, orange and red spheres, respectively. The table shows the properties of  $\text{CuBi}_2\text{O}_4$  relevant for PEC applications. b) IPCE spectra for  $\text{CuBi}_2\text{O}_4$  and  $\text{CuBi}_2\text{O}_4/\text{Pt}$  electrodes at 0.6 V versus RHE in 0.3 M  $\text{K}_2\text{SO}_4$  and 0.2 M phosphate buffer solution (pH 6.65), either purged with Ar or after  $\text{H}_2\text{O}_2$  addition. The dashed line represents the maximum IPCE values that can be reached based on the absorption spectra. Reproduced with permission.<sup>[94]</sup> Copyright 2016, American Chemical Society. c) Linear sweep voltammogram under 1 sun transient illumination at  $10 \text{ mV s}^{-1}$  of a  $\text{CuFeO}_2/\text{FTO}$  electrode in 1 M NaOH purged with Ar (red line) and  $\text{O}_2$  (blue line). Reproduced with permission.<sup>[114]</sup> Copyright 2015, Wiley-VCH. d) Proposed energy band diagram for an isolated  $\text{CuFeO}_2$  electrode in the dark. Reproduced with permission.<sup>[115]</sup> Copyright 2017, American Chemical Society.

IPCE value of  $\approx 8\%$  was reached at 400 nm. Likewise,  $\text{H}_2$  gas was detected by irradiating at  $\lambda > 420 \text{ nm}$ , and a Faradaic efficiency of 77% was determined.

## 2.2. Delafossites

Delafossite-type oxides are compounds with the formula  $\text{ABO}_2$ , where A and B are metals with oxidation states +1 and +3. They have a layered structure with a sheet of linearly coordinated A cations and layers of  $\text{BO}_6$  octahedra sharing edges. The structure is shown in Figure 3b for the mineral delafossite,  $\text{CuFeO}_2$ . Concretely, Cu(I) based delafossites have received considerable attention in the field of transparent conductive oxides (TCOs)<sup>[110–112]</sup> for optoelectronic devices. Most of them are wide bandgap semiconductors, such as  $\text{CuYO}_2$ ,  $\text{CuAlO}_2$ ,  $\text{CuGaO}_2$ , or  $\text{CuInO}_2$ , and exhibit high transparency and carrier mobility. Only a limited number of Cu(I) delafossites have bandgaps sufficiently

narrow for PEC applications, being among them  $\text{CuFeO}_2$  and  $\text{CuRhO}_2$ . Their high stability in aqueous media is a major advantage of Cu(I) delafossites, since this is one of the current challenges for achieving a practical device.

$\text{CuFeO}_2$  is the most studied delafossite for water photosplitting since, in 2012, Read et al.<sup>[113]</sup> reported the first study about the use of a  $\text{CuFeO}_2$  film deposited on an FTO transparent substrate as a photoelectrode. In that work, a new electrodeposition route was developed to prepare thin compact films with a bandgap of 1.55 eV. The authors highlighted the thermodynamic feasibility to produce  $\text{H}_2$  on this material under illumination while absorbing the entire range of the visible spectrum and delivering IPCE values up to 2% (at 350 nm). Later, Prévot et al.<sup>[114]</sup> reported on a sol-gel citrate-nitrate based technique to prepare  $\text{CuFeO}_2$  thin films that presents several advantages compared with electrodes synthesized via electrodeposition, such as straightforward solution processing of the films or the ability

to tune the layer thickness. Using an electron scavenger such as  $O_2$ , the photocurrents were reasonably large and stable for days. Conversely, the photoresponse for  $H_2O$  reduction was low (Figure 5c), which was attributed to both poor charge separation and transport properties, and sluggish charge transfer at the semiconductor/electrolyte interface. Later, the same authors reported a high mobility ( $0.2\text{ cm}^2\text{ V}^{-1}\text{ s}^{-1}$ ) and a relatively long lifetime (200 ns) for the photogenerated carriers.<sup>[115]</sup> Thus, they concluded that the limitation of the photoactivity is linked to the presence of a high density of surface states ( $10^{14}\text{ cm}^{-2}$ ) acting as electron traps (Figure 5d), promoting charge recombination and causing FLP at the surface. Alternatively, Jaegermann and co-workers, claimed that FLP due to the formation and occupation of the bulk  $Fe^{3+}/Fe^{2+}$  electron polaron level precludes  $CuFeO_2$  to develop the photovoltage for reaching the water reduction potential.<sup>[116]</sup> In a subsequent work, an IMPS analysis revealed that although bulk recombination was an important loss, the performance bottleneck for hydrogen production of  $CuFeO_2$  electrodes synthesized by aerosol-assisted chemical vapor deposition is surface recombination.<sup>[117]</sup> Many other reports have appeared in the last years pursuing both higher photoelectrochemical activity by using different synthetic routes and an in-depth understanding of the PEC performance of this material.<sup>[118–124]</sup> Despite the low photocurrents reported for water reduction, the material keeps on attracting interest owing to the Earth abundance of the constituent elements, narrow bandgap, high charge carrier mobility, and excellent stability in aqueous media under the typical conditions of applied potential and solution pH used in the experiments.<sup>[125]</sup> This has motivated the development of different strategies to overcome the barriers for water reduction, which will be commented in Section 3.

On the other hand, p-type  $CuRhO_2$ , with a bandgap of 1.9 eV, was also investigated as a photocathode under visible irradiation.<sup>[126]</sup>  $H_2$  was produced when using 1 M NaOH solutions purged with either air or Ar. The authors concluded that water photoreduction was preferred over oxygen photoreduction on this material. In addition, the photoelectrode tended to corrode under illumination in an Ar-purged electrolyte with the formation of Cu(0) (detected by XPS) while in the presence of  $O_2$ , Cu(0) was not detected. In the latter case, the measured Faradaic efficiency for hydrogen generation was  $\approx 80\%$ . Later, the same group also tested p- $AgRhO_2$  as a photocathode for HER, showing even higher photocurrents and photostabilities than  $CuRhO_2$ . The faradaic efficiency was around 95% from pH 0 to 14.<sup>[127]</sup> However, despite the suitable properties as photocathodes of Rh oxides (see also  $ZnRh_2O_4$ , Section 2.1), the practical use of materials containing platinum-group metals is compromised due to their scarcity and, consequently, their high cost.

Wide-bandgap delafossite materials have also been examined for PEC water splitting. Besides  $CuGaO_2$ ,<sup>[128]</sup> Díaz-García et al.<sup>[129]</sup> inspected the photoelectrochemical properties of  $CuCrO_2$  delafossite thin films prepared by a sol gel route. Although the material bandgap is too wide to absorb in the visible range (3.15 eV) of the solar spectrum, the IPCE attained values near 6% at 350 nm, which is remarkably high compared with other p-type oxide materials. It is also worth noting the excellent stability of the photoresponse in both acidic and alkaline media.

### 2.3. Perovskites

Perovskite type oxides are compounds with the formula  $ABO_3$ , where A and B are metals with different combinations of oxidation states ( $A^{+1}$  and  $B^{+5}$ ,  $A^{+2}$  and  $B^{+4}$ ,  $A^{+3}$  and  $B^{+3}$ ). The ideal structure is a cubic lattice (Figure 3c) consisting of small B cations in oxygen octahedra and larger A cations coordinated by 12 O atoms. Commonly these materials present a distortion of the lattice leading to other variants with lower symmetry, such as the orthorhombic or hexagonal structures.<sup>[130,131]</sup> It is worth noting that ilmenite oxides have the same stoichiometry, (i.e.,  $ABO_3$ ). The prevalence of the perovskite or ilmenite structures depends on the ratio between the ionic radii of the constituent metals.<sup>[132]</sup>

To the best of our knowledge, the first works regarding perovskite oxides as photocathodes were released in 1980 by Jarret et al.<sup>[133,134]</sup> They constructed an electrolytic cell that produced hydrogen without applying external bias using p-type  $LuRhO_3$  as a photocathode and  $TiO_2$  as a photoanode. Despite the long time elapsed from the publication of this paper, further relevant work on  $LuRhO_3$  as a photocathode has not appeared. In 1987, a preliminary study of the photoelectrochemical behavior of  $LaCoO_3$  was published.<sup>[135]</sup> More recently, the group of Maggard studied for the first time the photoelectrochemistry and electronic structure of  $CuNbO_3$ .<sup>[136]</sup> Photoelectrodes were prepared by the doctor blade technique from presynthesized pure  $CuNbO_3$  powders. In Ar-purged  $Na_2SO_4$  solution, the IPCE reached rather high values, exceeding 5%. Its absorption extends to the visible range (optical bandgap  $\approx 2.0\text{ eV}$ ), although the onset of the photocurrent was not too positive ( $\approx 0.7\text{ V}$  vs RHE). The excellent stability of the photocurrent (over several hours) when applying significant bias is remarkable.

Lanthanide iron perovskites, such as  $LaFeO_3$ ,<sup>[137–141]</sup>  $NdFeO_3$ ,<sup>[142]</sup> and  $PrFeO_3$ <sup>[143]</sup> have emerged as photocathodes for PEC in recent years since Celorrio et al.<sup>[137]</sup> reported a nanostructured  $LaFeO_3$  electrode as a photocathode for the first time. In that work, high purity powders were prepared by a novel ionic-liquid-based method and then screen printed, resulting in thick nanoparticulate films. Despite cathodic photocurrents start appearing at 1.1 V versus RHE, the photoresponse for HER was modest. Based on this work, Yu et al.<sup>[138]</sup> fabricated 100 nm-thick film electrodes over a conductive substrate by PLD. They were able to construct a p- $LaFeO_3/n-Fe_2O_3$  photocell detecting  $H_2$  and  $O_2$  with a ratio of nearly 2:1 and stable photoresponse, at least for 120 h, using visible light but with the application of a significant bias. More recently, thin film  $LaFeO_3$  electrodes were synthesized at  $640\text{ }^\circ\text{C}$  by a sol gel method combined with spin coating over an FTO substrate.<sup>[139]</sup> The photoelectrodes exhibited low photocurrents in an  $N_2$ -purged electrolyte, which dramatically increased in the presence of  $O_2$  as an electron scavenger. A similar behavior was observed by Liu et al.<sup>[144]</sup> and Freeman et al.<sup>[145]</sup> using different synthetic methods, not only for  $LaFeO_3$ , but also for  $NbFeO_3$  thin films.<sup>[142]</sup> The need for modification of the material in order to overcome the sluggish charge transfer to water is apparent. Moreover,  $YFeO_3$  photoelectrodes have been studied as both amorphous and nanostructured thin film electrodes, being the temperature for the crystallization of the material higher than in the case of  $LaFeO_3$ .<sup>[146]</sup> Despite the photocathodic behavior, for both types of



electrodes, the photocurrents were very low, revealing poor charge transport across the films. Besides the photocathodic behavior of LaFeO<sub>3</sub> photoelectrodes described above, it must be emphasized that several authors have reported anodic photocurrents for this material.<sup>[147–153]</sup> This suggests that the electrical properties of the material critically depend on the synthesis procedure, which can lead to different types of impurities and defects.

BiFeO<sub>3</sub> can also exhibit n- or p-type behavior, being mostly described as a photoanode.<sup>[154–156]</sup> Among others,<sup>[157–161]</sup> Gu et al.<sup>[160]</sup> obtained a BiFeO<sub>3</sub> film on a transparent conductive substrate behaving as a photocathode with a bandgap of 2.3 eV. Photocurrent–potential curves showed an onset potential of 0.75 V versus RHE in 0.1 M Na<sub>2</sub>SO<sub>4</sub> aqueous electrolyte and low photocurrents (IPCE 0.21% at 400 nm) for the bare material. More recently, Ge et al.<sup>[162]</sup> showed a photocathodic behavior for BaBiO<sub>3</sub> electrodes. They compared compact electrodes obtained by a sol-gel method and nanoporous electrodes prepared by screen printing. The latter showed the best performance, reaching 1 mA cm<sup>-2</sup> at 0 V versus RHE with one sun illumination, but they suffered from photocorrosion.

#### 2.4. Other Ternary Oxides

Other ternary oxide materials cannot be classified into one of the above structural groups. One of them is Sr<sub>7</sub>Fe<sub>10</sub>O<sub>22</sub>, which was reported by Matsumoto et al. in 1987 together with CaFe<sub>2</sub>O<sub>4</sub>,<sup>[77]</sup> as a new photocathodic material for hydrogen evolution. Quantum efficiencies up to 10% were attained with visible light, but the authors stated that the photocurrents were not very stable in a long-term test.

Cu-based vanadates, tantalates, and niobates have been mainly explored by the group of Maggard.<sup>[46]</sup> Cu(I) tantalates present the general formula Cu<sub>x</sub>Ta<sub>3n+1</sub>O<sub>8n+3</sub>. Their structure consists of layers of TaO<sub>7</sub> pentagonal bipyramids alternating with layers of linearly coordinated Cu(I) and TaO<sub>6</sub> octahedra.<sup>[87]</sup> Films of p-type semiconducting Cu<sub>5</sub>Ta<sub>11</sub>O<sub>30</sub> and Cu<sub>3</sub>Ta<sub>7</sub>O<sub>19</sub><sup>[163,164]</sup> exhibit IPCE values of 1–2% for 500–600 nm. Different Cu niobates have been tested as photocathodes for HER such as CuNbO<sub>3</sub>,<sup>[136]</sup> CuNb<sub>3</sub>O<sub>8</sub>,<sup>[165]</sup> CuNb<sub>2</sub>O<sub>6</sub>,<sup>[166]</sup> and Cu<sub>2</sub>Nb<sub>8</sub>O<sub>21</sub>,<sup>[167]</sup> and also for CO<sub>2</sub> reduction.<sup>[166,168]</sup> Specifically, CuNb<sub>3</sub>O<sub>8</sub> was prepared by means of presynthesized powders coated on an FTO substrate.<sup>[165]</sup> The photoelectrochemical properties were measured at pH 6.3 reaching IPCE values around 6% at 400 nm and Faradaic efficiencies for hydrogen generation of 62%. This material exhibits a high hole mobility (145 cm<sup>2</sup> V<sup>-1</sup> s<sup>-1</sup>), but a low acceptor density (≈7 × 10<sup>15</sup> cm<sup>-3</sup>). Regarding copper vanadates, Cu<sub>3-x</sub>VO<sub>4</sub> was reported to have a narrow bandgap of 1.2 eV.<sup>[169]</sup> Recently, Song et al.<sup>[170]</sup> reported thin film p-type Cu<sub>5</sub>V<sub>2</sub>O<sub>10</sub> obtained by spray pyrolysis, having a bandgap of 1.8–2.0 eV. Moderate absorption properties and extensive charge trapping preventing the photogenerated carriers from reaching the interface are linked to the low photocurrents detected. In addition, copper reduction and dissolution cause poor chemical stability. In general, these Cu-based materials exhibit narrow bandgaps (as low as 1.2 eV) and large initial photocurrents, but their stability over time should be improved.

Ca<sub>2</sub>Fe<sub>2</sub>O<sub>5</sub> has been recently examined as a photocathode, showing a relatively narrow bandgap of 2.1 eV.<sup>[171]</sup> That work stands out because it is the first devoted to a brownillerite-type material in PEC research. Ca<sub>2</sub>Fe<sub>2</sub>O<sub>5</sub> photoelectrodes were achieved by drop-casting a Ca<sup>2+</sup> solution on a FeOOH film, and then heating at 650 °C. The electrodes show an onset potential as positive as 1.22 V versus RHE for water reduction, and 1.36 V for O<sub>2</sub> reduction, with the drawback that the material is not completely photostable.

### 3. Strategies for Improving Photoelectrochemical Performance

The overall PEC water splitting reaction can be considered to involve three main steps: (i) light absorption by the semiconductor to generate electron–hole pairs, (ii) charge separation and transport (migration/diffusion) of the minority charge carriers to the semiconductor surface (and the majority charge carriers to the back contact), and (iii) charge transfer at the semiconductor/electrolyte interface for water reduction or oxidation. Engineering the electrode is a primary component of the research aiming to improve the performance of the materials to obtain an efficient and durable solar water splitting device. As reviewed in the above section, bare TMOs suffer from serious issues that limit the H<sub>2</sub> generation efficiency. Overall, the most common approaches adopted in photoelectrode design<sup>[172,173]</sup> to tackle such shortcomings (**Figure 6**) are: (i) Increasing light absorption by engineering the electronic structure of the semiconductor through doping, by the modulation of the material architecture, or through dye sensitization. (ii) Enhancing majority charge carrier collection in the back contact by creating heterojunctions, or by increasing the conductivity through doping. (iii) Diminishing surface recombination and/or increasing minority carrier extraction by depositing passivation or extracting layers. (iv) Increasing the rate of charge carrier transfer to the electrolyte by nanostructuring the material or attaching a surface cocatalyst. (v) Improving the stability of the material (reducing photocorrosion) by loading protective layers.

The organization of this section will be based on the strategies employed to improve PEC water splitting according to the different steps of the process as stated previously. For each one, the rationale behind the strategies is described together with a revision of the most relevant achievements, emphasizing those linked to TMOs as photocathodes. The stability issue is usually linked to other strategies that affect the semiconductor surface, such as heterojunctions, passivation layers and deposition of cocatalysts, and consequently they are addressed concomitantly with the other effects. At the end of the section, **Table 2** includes some relevant reports on TMO PEC improvement by modification according to these strategies.

#### 3.1. Improving Light Absorption through Doping, Nanostructure Engineering, and Dye Sensitization

One important challenge in finding a photoelectrode meeting the requirements specified in the introductory part is that the materials demonstrating high (photo)electrochemical stability usually have too wide bandgaps, the most popular example being that of

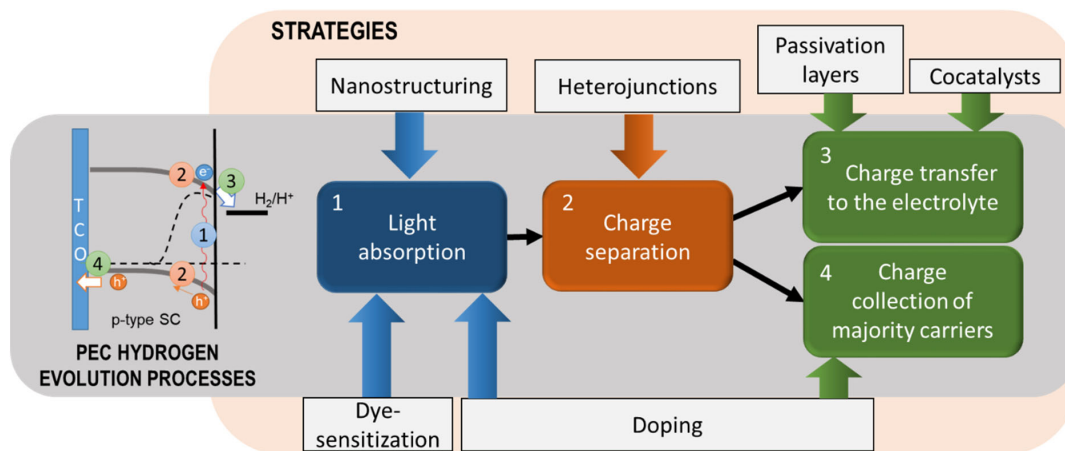


**Figure 6.** Scheme showing potential strategies employed in TMO photocathodes for improving the different photoelectrochemical hydrogen evolution steps.

TiO<sub>2</sub>. Materials with poor absorption in the visible range of the solar spectrum have a limited use in PEC applications. To overcome this limitation, two main approaches are adopted when the material possesses a wide bandgap. First, doping to produce extra energy levels within the forbidden gap that may enhance visible light absorption. The drawback is that these states can also act as recombination centers, bringing in new recombination routes. Most of the studies exploring this strategy were targeted on TiO<sub>2</sub>. It is reported that the introduction of C, N, and S as dopants in TiO<sub>2</sub> provide additional electronic states above the valence band edge, producing a red-shift absorption.<sup>[174]</sup> Second, sensitizing a wide bandgap semiconductor with a dye also enhances light harvesting. Dye-sensitized photoelectrochemical cells (DSPECs) emerged from the idea of the widely studied dye-sensitized solar cells (DSCs). In this approach, a dye (sensitizer) is loaded at a mesoporous semiconductor surface and allowed to induce a photocurrent using photons with energy lower than the semiconductor bandgap.<sup>[175]</sup> In this case, the dye absorbs the visible light, charge separation takes place at the dye/semiconductor interface and charge transport mainly occurs through the semiconductor (and electrolyte). This strategy has been widely employed in the case of TiO<sub>2</sub> photoanodes for over 20 years, while for photocathodes most of the works have focused on NiO.<sup>[176]</sup>

The generation of nanostructures is another widely used strategy in photoelectrochemistry. Among the potential advantages of nanostructures are the shorter carrier collection path and the improvement of light absorption induced by scattering. In contrast, in some nanostructures surface recombination can increase because of a larger interfacial area, lack of a fully developed space charge layer (charge carriers move by diffusion rather than by drift) and slow interparticle charge transport. These disadvantages are partly reduced in quasi-1D and -2D structures such as nanocolumns, nanoflakes, etc. Photonic nanostructures can also help to confine light and, thus, enhance light absorption.

### 3.1.1. Shift of the Absorption Edge

In the case of TMOs, some works have shown an enhancement of light absorption by the introduction of a third metal in the

structure (doping). In this way, doping SrTiO<sub>3</sub> with rhodium<sup>[177,178]</sup> not only switches the n-type character of pristine SrTiO<sub>3</sub> to p-type (further explained in the next section), but also increases the absorption coefficient in the visible region. Iwashina et al.<sup>[177]</sup> established that an absorption band appearing at ≈400 nm is related to electronic transitions from electron-donor levels consisting of Rh<sup>3+</sup>, while another absorption band at ≈600 nm is linked to transitions involving acceptor levels consisting of Rh<sup>4+</sup>. A red-shift of the absorption edge from 2.11 to 1.97 eV has been reported for ZnFe<sub>2</sub>O<sub>4</sub> upon doping with Co.<sup>[88]</sup> K-doping was also shown to decrease the bandgap of LaFeO<sub>3</sub> by about 0.2 eV by lowering the energy of the CB edge.<sup>[179]</sup> Very recently, a rather similar effect was reported upon Li doping in LaFeO<sub>3</sub>.<sup>[180]</sup> Conversely, the introduction of Ta in CuNbO<sub>3</sub> photoelectrodes yields a small blue shift of the bandgap, although this effect does not produce a significant impact on the photocurrent values.<sup>[181]</sup>

### 3.1.2. Dye Sensitization

Recently, dye sensitization has been reported for CuGaO<sub>2</sub>,<sup>[182]</sup> CuCrO<sub>2</sub>,<sup>[183]</sup> and LaFeO<sub>3</sub><sup>[184]</sup> photocathodes. Kumagai et al.<sup>[182]</sup> fabricated a new hybrid composed of CuGaO<sub>2</sub> with a Ru(II)-Re(I) supramolecular photocatalyst that outperforms the photoactivity for CO<sub>2</sub> reduction to CO reported in a previous work using NiO instead of the ternary oxide. Regarding H<sub>2</sub> photogeneration, Reisner and co-workers<sup>[183]</sup> used for the first time CuCrO<sub>2</sub> after co-immobilization of a phosphonated diketopyrrolopyrrole dye and a Ni-bis(diphosphine) catalyst. The hybrid photoelectrode shows a photocurrent onset potential of +0.75 V versus RHE. On the other hand, LaFeO<sub>3</sub> was employed together with a molecular dye (P1\*) and a NiP catalyst, doubling in this way the photocurrent of the bare electrode.<sup>[184]</sup> In this case, both LaFeO<sub>3</sub> and P1\* absorb visible light. Li et al. also achieved an improvement of the photoresponse by sensitizing CuFe<sub>2</sub>O<sub>4</sub> nanostructured electrodes with a porphyrinato-manganese complex.<sup>[185]</sup> These works have paved the way for the application of dye sensitization not only

**Table 2.** Review of the main strategies employed in ternary oxide photocathodes and the evidences of the improvement in the photoelectrochemical performance.

Material	Strategy	Evidences of PEC improvement	Ref.
CaFe <sub>2</sub> O <sub>4</sub>	Metal doping with Ag, Au and CuO	Ag doping leads to the best photoresponse. IPCE ≈0.3% for undoped and 2% for doped (at 420 nm in O <sub>2</sub> -purged 0.2 M K <sub>2</sub> SO <sub>4</sub> ).	[215]
CaFe <sub>2</sub> O <sub>4</sub>	Doping with Na and Mg	The photocurrent increases from ≈0.35 to 1.4 mA cm <sup>-2</sup> (in 0.1 M H <sub>2</sub> SO <sub>4</sub> ) after the introduction of Na and Mg.	[212]
CuBi <sub>2</sub> O <sub>4</sub>	CuBi <sub>2</sub> O <sub>4</sub> /Pt	IPCE increases from ≈2% to ≈9% after Pt loading (in pH 6.65 at 400 nm).	[94]
	Doping with Ag: CuBi <sub>2</sub> O <sub>4</sub> /Ag-doped CuBi <sub>2</sub> O <sub>4</sub>	Increase of the photocurrent values. IPCE of ≈4.5% for Ar-purged and ≈8.5% in O <sub>2</sub> -purged 0.1 M NaOH (at 400 nm) for the doped electrodes.	[93]
	Heterojunction + cocatalyst, Pt: CuO/CuBi <sub>2</sub> O <sub>4</sub> /Pt	CuO/CuBi <sub>2</sub> O <sub>4</sub> /Pt doubles the photocurrent for the homo-layered electrodes (also with Pt). IPCE higher than 30% (in pH 6.8 at 400 nm).	[208]
	Au underlayer FTO/Au/ CuBi <sub>2</sub> O <sub>4</sub>	Increase of the photocurrents from 0.23 to 1.2 mA cm <sup>-2</sup> at 0.1 V versus RHE in 0.1 M Na <sub>2</sub> SO <sub>4</sub>	[96]
	Heterostructure with polythiophene CuBi <sub>2</sub> O <sub>4</sub> /PTh	Increase of the IPCE from 4 to 6% at 400 nm	[205]
	CuBi <sub>2</sub> O <sub>4</sub> /NiO heterojunction	Photocurrent increase from 1 mA cm <sup>-2</sup> for the bare CuBi <sub>2</sub> O <sub>4</sub> to 1.5 mA cm <sup>-2</sup> for the CuBi <sub>2</sub> O <sub>4</sub> /NiO at 0.4 V vs RHE	[200]
	CuBi <sub>2</sub> O <sub>4</sub> /Graphene oxide (GO)	Two-fold enhancement in the photocurrent in CuBi <sub>2</sub> O <sub>4</sub> /GO with respect to the CuBi <sub>2</sub> O <sub>4</sub> electrodes.	[199]
	CuBi <sub>2</sub> O <sub>4</sub> /TiO <sub>2</sub> (protective layer)	Enhanced photocurrent stability in both neutral and alkaline media.	[202]
	CuO/CuBi <sub>2</sub> O <sub>4</sub> heterojunction + loading Pt as cocatalysts	Photocurrent at 0.4 V vs RHE changes from 1.16 to 2.8 mA cm <sup>-2</sup> upon the CuO/CuBi <sub>2</sub> O <sub>4</sub> heterostructure formation and to 3.5 mA cm <sup>-2</sup> after Pt loading.	[108]
	Cu:NiO back contact (FTO/Cu:NiO/CuBi <sub>2</sub> O <sub>4</sub> )	Increase of the photocurrent density at 0.6 V vs RHE from 2.26 to 2.83 mA cm <sup>-2</sup> in presence of H <sub>2</sub> O <sub>2</sub> .	[207]
	CuBi <sub>2</sub> O <sub>4</sub> /Pt	Increase of IPCE values from ≈13% to ≈20% after Pt loading	[104]
CuFeO <sub>2</sub>	Heterojunction + cocatalyst, Pt: CuFeO <sub>2</sub> /AZO/TiO <sub>2</sub> /Pt	A large increase of the photocurrents up to 0.8 mA cm <sup>-2</sup> (Ar-purged buffer electrolyte at pH 6.1), albeit with onset shift toward negative values, from 0.9 to 0.4 V vs RHE.	[114]
	Oxidative heat treatment	Two-fold increase of the acceptor density. Photocurrents double in 2-layer electrodes after the oxidation at 300 °C for 1 h.	[114]
	Scaffold CuAlO <sub>2</sub> layer	Photocurrents 2.5-fold higher with the composite (in O <sub>2</sub> -purged 1 M NaOH).	[206]
	Hybrid microwave annealing (HMA) + NiFe-layered double hydroxide/reduced graphene oxide electrocatalyst	HMA treatment produces an increase of the photocurrent at 0.4 V vs RHE more than 4 times (1.3 mA cm <sup>-2</sup> at 0.4 V vs RHE) with respect to the untreated electrode. After NiFe LDH/ RGO electrocatalyst loading the photocurrent increases to 2.4 mA cm <sup>-2</sup> .	[216]
	2D opals structure, CuAlO <sub>2</sub> /CuFeO <sub>2</sub> heterojunction	9-fold enhancement of the photocurrent density at 0.6 V vs RHE in presence of O <sub>2</sub> , for the CuFeO <sub>2</sub> /CuAlO <sub>2</sub> double-shelled structure with respect to the single shelled counterpart	[119]
	Inverse opal structures (IO) + C <sub>60</sub> /CoFe LDH cocatalyst	The IO CuFeO <sub>2</sub> yielded a photocurrent of 4.86 mA cm <sup>-2</sup> at 0 V vs RHE, which is more than twice the HER performance of the planar one (both after electrocatalyst deposition). The C <sub>60</sub> /CoFe LDH electrocatalyst improved the photocurrent by a factor of 4.6 compared with the bare IO CuFeO <sub>2</sub> photocathode.	[121]
CuNbO <sub>3</sub>	Oxidative heat treatment	Increase of the photocurrents after the oxidation at 250–350 °C for 3 h.	[181]
Cu <sub>3</sub> Ta <sub>7</sub> O <sub>19</sub>	Oxidative heat treatment	Increase of the photocurrent after the heat treatment at 350 and 550 °C for 3 h.	[163]
Cu <sub>5</sub> Ta <sub>11</sub> O <sub>30</sub>	Oxidative heat treatment	The photocurrents increase dramatically after the heat treatment at 250–350 °C for 3 h.	[163]
Cu <sub>5</sub> Ta <sub>11</sub> O <sub>30</sub>	Oxidative heat treatment	Increase of the photocurrent after the heat treatment at 350–550 °C for 15–60 min.	[164]

**Table 2.** Continued.

Material	Strategy	Evidences of PEC improvement	Ref.
Cu <sub>3</sub> VO <sub>4</sub>	Oxidative heat treatment	Decrease of dark currents and increase of photocurrent after an oxidative treatment (300–350 °C 15 min).	[169]
LaFeO <sub>3</sub>	Doping with Mg and Zn	Six-fold enhancement of the photocurrent by doping with a 5 at% with Mg or Zn (respect to the Fe amount)	[139]
	Doping with K	Cathodic photocurrent more than doubles at 0.6 V vs RHE for K-doped LaFeO <sub>3</sub> electrodes in O <sub>2</sub> -saturated solution. Bandgap decreases from 2.2 eV (undoped) to 2.0 eV (K-doped)	[179]
	Doping with Mg, Ca, Sr and Ba	Photocurrent increase upon alkaline-earth cation substitution in O <sub>2</sub> -saturated electrolyte.	[213]
	Doping with Li	Increase of the cathodic photocurrent from 30 to 50 μA cm <sup>-2</sup> at 0.4 V vs RHE and bandgap decrease from 2.14 to 2.00 eV.	[180]
NdFeO <sub>3</sub>	Doping with Mg and Zn	The photocurrents multiply by factors of 3.4 and 2.8 for the Mg and Zn-doped NdFeO <sub>3</sub> (5 at%) for O <sub>2</sub> -purged electrolyte.	[142]
SrTiO <sub>3</sub>	Doping with Rh	Cathodic photocurrents increase with the Rh content, up to an optimum for SrTiO <sub>3</sub> :Rh (7 at%). Faradaic efficiency of 100%.	[177]
SrTiO <sub>3</sub>	Doping with Rh: Rh <sup>4+</sup> and Rh <sup>3+</sup>	Photocurrent onset 0.6 V more positive for Rh <sup>3+</sup> :SrTiO <sub>3</sub> than for Rh <sup>4+</sup> :SrTiO <sub>3</sub> .	[178]
ZnFe <sub>2</sub> O <sub>4</sub>	Doping with Co	Photocurrent enhanced 7.33 times at 0 V vs RHE for the Co-ZnFe <sub>2</sub> O <sub>4</sub> electrode.	[88]
ZnRh <sub>2</sub> O <sub>4</sub>	p–n junction: ZnO/ZnRh <sub>2</sub> O <sub>4</sub>	IPCE increases from ≈8% ZnRh <sub>2</sub> O <sub>4</sub> to ≈13% for ZnO/ZnRh <sub>2</sub> O <sub>4</sub> (at 400 nm) in Ar-purged 0.1 M Na <sub>2</sub> SO <sub>4</sub> at 0 V vs RHE.	[109]

for the HER, but also for the photoelectrochemical production of other fuels.

### 3.1.3. Light Absorption Improvement by Scattering

Opal inverse nanostructures have been demonstrated to be effective for enhancing light absorption as they favor multiple scatterings within the nanostructure and provide a shorter pathway for the majority carriers to be collected, diminishing recombination.<sup>[186–188]</sup> Very recently, Oh et al.<sup>[121]</sup> prepared CuFeO<sub>2</sub> inverse opal electrodes using polystyrene microspheres as templates with superior PEC performance compared with a planar electrode prepared by sol-gel (Figure 7a–f). They observed enhanced light absorption in the inverse opal electrodes with respect to the planar electrodes owing to an increase of the scattering near the band edge of the material together with a more efficient transfer (to produce H<sub>2</sub>) of the visible-light-induced electrons, leading to an improved PEC performance (Figure 7g). Another strategy followed by Oh et al.<sup>[118]</sup> was based on a 2D photonic crystal architecture that acts as a self-light-harvester. They fabricated an electrode composed of CuFeO<sub>2</sub>-decorated silica microspheres that simultaneously shows a high transmittance of 76.4% and relatively high photoresponse.

## 3.2. Improving Charge Carriers Separation and Stability by Heterojunctions

In this methodology, a single-semiconductor photoelectrode is brought in contact with another one forming a heterojunction, which is the junction between two semiconductors having different bandgaps. A proper band alignment between them can be beneficial for the separation of the photogenerated charge carriers, improving the PEC efficiency. Heterojunctions are

classified into several types,<sup>[1]</sup> but the most frequently employed for improving the PEC performance is the so-called type II p–n junction (Figure 8a). In this type of contact, electrons diffuse across the junction to the p-type region, and holes diffuse to the n-type region until reaching equilibrium. This process causes a lack of charge neutrality near the contact between both materials, creating a positively charged region on the n-type side and a negatively charged region in the p-type side, generating a depletion region. Rectification occurs at the interface between both semiconductors, and ideally electrons can flow only in one direction (from the p-type to the n-type semiconductor). Heterojunctions have been previously studied in the field of photocatalysis.<sup>[189]</sup> Regarding PEC applications, the most common approach is the direct deposition of a second semiconductor on the first semiconductor surface, however, in some cases the second semiconductor can also be formed by the direct reaction of the TMO, typically leading to a binary oxide. Some p-type TMOs have been employed for forming heterojunctions in photoanodes, as is the case of CaFe<sub>2</sub>O<sub>4</sub> in combination with n-type BiVO<sub>4</sub>,<sup>[190,191]</sup> α-Fe<sub>2</sub>O<sub>3</sub><sup>[192]</sup> or TaON,<sup>[193]</sup> CuFe<sub>2</sub>O<sub>4</sub> on WO<sub>3</sub>,<sup>[194]</sup> and LaFeO<sub>3</sub> on ZnO.<sup>[195,196]</sup>

### 3.2.1. Heterojunctions with n-Type Materials

Generally, this approach consists in the deposition of an n-type semiconductor overlayer over a p-type semiconductor, forming a type II heterojunction. Apart from the rectifying effect, an overlayer of a particular material can also suppress other competitive processes associated with photocorrosion of the semiconductor or surface recombination of photogenerated electron-hole pairs, thus improving the PEC photoresponse and stability (passivation layers). It is worth noting that for very thin

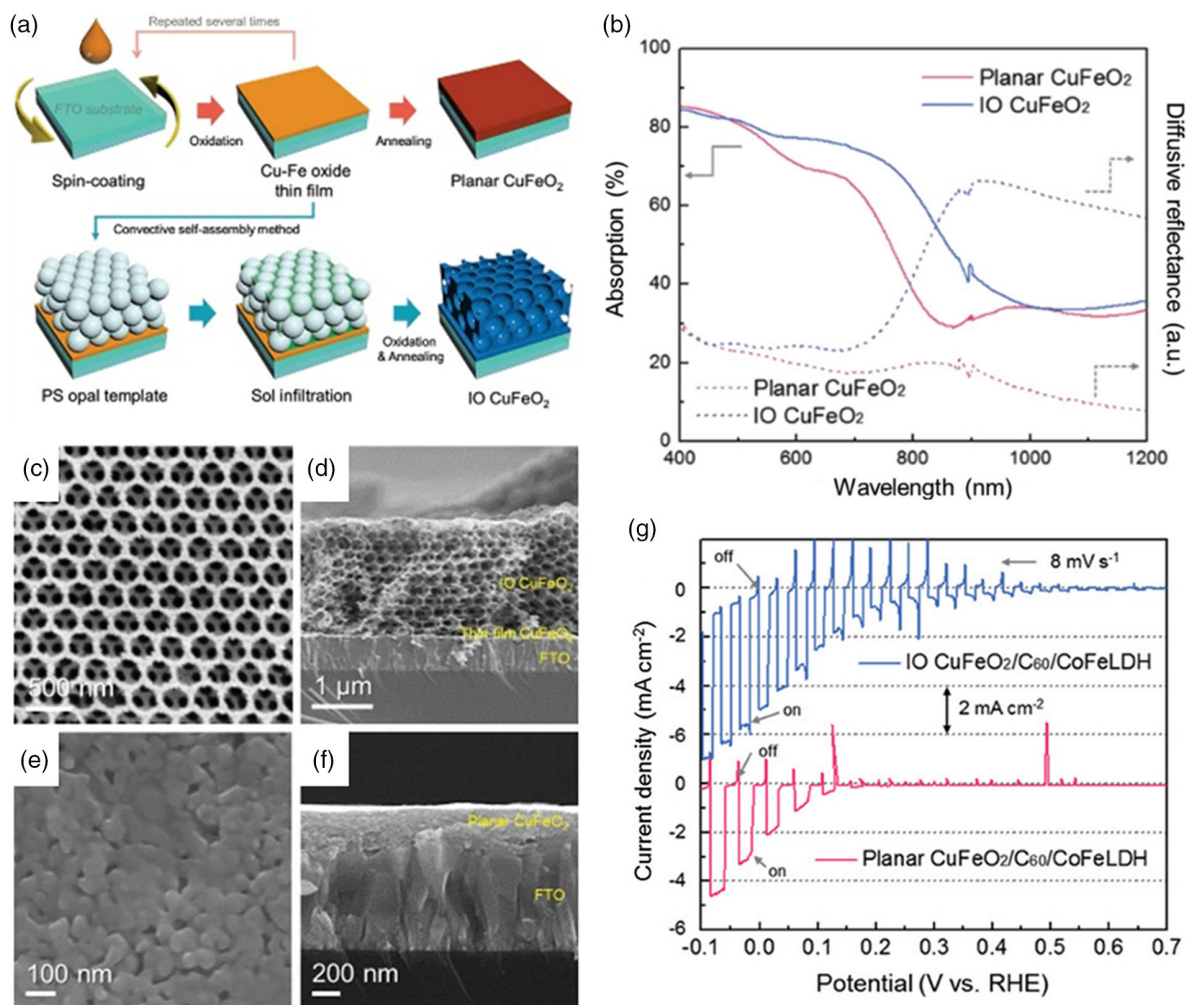


**Figure 7.** a) Scheme of electrode fabrication and b) absorption and diffusive reflectance spectra for planar and inverse opal (IO) FTO/CuFeO<sub>2</sub> electrodes. c, e) Top and d, f) cross-sectional SEM images of the c, d) inverse opal and e, f) planar electrodes. g) Linear sweep voltammogram with transient illumination in Ar-purged 1 M NaOH solution of the FTO/CuFeO<sub>2</sub> electrodes after modification with C<sub>60</sub>/CoFe. Reproduced with permission.<sup>[121]</sup> Copyright 2019, Wiley-VCH.

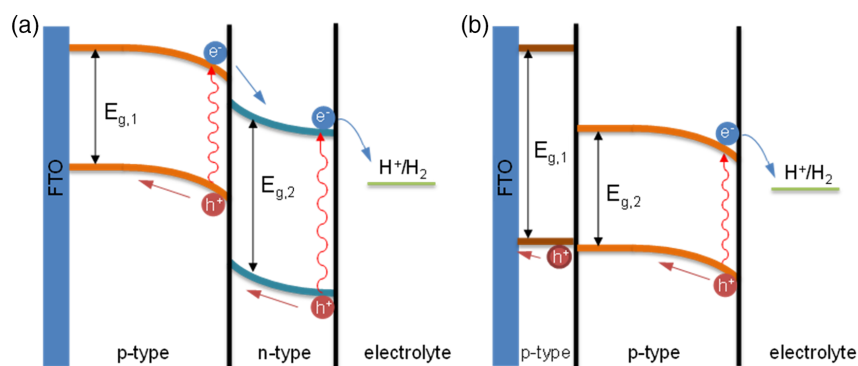


**Figure 8.** Band energy diagrams of junctions under photoexcitation showing the electron and hole flows in a photocathode for hydrogen evolution; a) p-n junction in which both materials absorb light irradiation being  $E_{g,1} < E_{g,2}$  and b) p-p junction in which only the uppermost semiconductor absorbs light irradiation and the thin film p-type underlayer helps to separate the charge carriers.

layers, <2 nm, tunneling effects can prevail in the charge transfer mechanism.<sup>[197]</sup>

In binary oxide photocathodes, the most relevant results dealing with the use of heterojunctions have been reported by the group of Graetzel using Cu<sub>2</sub>O as the absorber material. They have developed a method for both improving the photoresponse and protecting Cu<sub>2</sub>O from photocorrosion.<sup>[54,59,60,198]</sup> In their initial work, Paracchino et al.<sup>[54]</sup> revealed a threefold enhancement of the photocurrent for a Cu<sub>2</sub>O/21 nm ZnO/11 nm TiO<sub>2</sub>/Pt multilayer compared with a Cu<sub>2</sub>O/Pt electrode. The ZnO buffer probably provides a more uniform hydroxylated surface for TiO<sub>2</sub> growth, in addition to forming a rectifying junction with Cu<sub>2</sub>O. The introduction of ZnO/Al<sub>2</sub>O<sub>3</sub> multilayers greatly enhances the stability of the photocurrent with time. Similarly, Kamimura et al.<sup>[109]</sup> coated ZnO on p-type ZnRh<sub>2</sub>O<sub>4</sub> following a sol-gel method. The ZnO thin overlayer forms a space charge depletion region at the ZnRh<sub>2</sub>O<sub>4</sub>/ZnO interface (p–n heterojunction), which results in a more efficient separation of the charge carriers (besides improving the electrical contact between ZnRh<sub>2</sub>O<sub>4</sub> particles). This approach results in an IPCE value of ~13% at 400 nm, being ~8% for the untreated electrode. A number of studies have been performed for CuBi<sub>2</sub>O<sub>4</sub>, including layers formed of TiO<sub>2</sub>, NiO, Cu<sub>x</sub>Ti<sub>y</sub>O<sub>z</sub>, or graphene oxide.<sup>[199]</sup> A heterojunction with NiO was shown to increase the photocurrent from 1 to 1.5 mA cm<sup>-2</sup>.<sup>[200]</sup> Recently, Zhang et al. revealed that a Cu<sub>x</sub>Ti<sub>y</sub>O<sub>z</sub> overlayer has a passivation effect, suppressing carrier recombination and reducing FLP.<sup>[201]</sup> Overlayers of TiO<sub>2</sub> with thickness about 20 and 120 nm have been employed for CuBi<sub>2</sub>O<sub>4</sub> electrodes as protective layers to mitigate photocorrosion.<sup>[100,103,202]</sup> Specifically, Berglund and co-workers<sup>[103,203]</sup> employed a CdS/TiO<sub>2</sub> heterojunction as a conformal coating on CuBi<sub>2</sub>O<sub>4</sub> to mitigate photocorrosion, although the onset of photocurrent was shifted toward negative values. The formation of a type II junction in BiFeO<sub>3</sub>/Bi<sub>2</sub>O<sub>3</sub> improves charge separation and increases IPCE up to 2.6% at 365 nm.<sup>[204]</sup>

Other materials such as organic polymers can also be used in heterojunctions. For instance, the coating of a porous CuBi<sub>2</sub>O<sub>4</sub> nanostructure with transparent polythiophene (PTh) gives rise to an increase of the IPCE values from 4 to 6% at 400 nm because of the adequate location of the semiconductor band edges and the organic material HOMO and LUMO levels.<sup>[205]</sup>

### 3.2.2. Heterojunctions with Other p-Type Materials

Following a similar approach to that of Figure 8a, charge separation can be facilitated by the heterojunction of two p-type materials with adequate relative band edge locations. A common approach is combining a thin layer of a wide bandgap oxide with a narrow bandgap semiconductor, the latter acting as a visible-light absorber material (Figure 8b), for a more effective extraction of majority carriers. This strategy was used by Prévot et al.<sup>[206]</sup> through the introduction of a wide-bandgap mesoporous p-CuAlO<sub>2</sub> semiconductor (scaffold layer) between the FTO substrate and the light absorber film, p-CuFeO<sub>2</sub>. In that work, the optimization of the scaffold thickness resulted in a 2.4-fold increase of the photocurrent (Figure 9a) in the presence of O<sub>2</sub>, while the onset potential remained unaltered. The composite electrode presents higher IPCE values over the entire wavelength

range compared to the control CuFeO<sub>2</sub> electrode (Figure 9b). The authors suggested that a selective extraction of the photogenerated holes toward the substrate at the CuFeO<sub>2</sub>/CuAlO<sub>2</sub> interface (Figure 9c) is due to the favorable band alignment between both materials. Analogously, Oh et al.<sup>[119]</sup> improved CuFeO<sub>2</sub>-shelled silica microspheres by the incorporation of a CuAlO<sub>2</sub> outer shell. Due to the improved charge separation, a ninefold increase of the photocurrent in the presence of O<sub>2</sub> was observed. The contact of CuFeO<sub>2</sub> with the electrolyte was facilitated by a partial etching of the silica microspheres (Figure 9d). IPCE values as high as 10% were reached at 400 nm (Figure 9e). This strategy was also applied to CuBi<sub>2</sub>O<sub>4</sub> electrodes by Berglund and co-workers. In this case, a Cu-doped NiO layer acts as a hole selective back contact, improving hole transport. The Cu:NiO layer reduces the barrier height at the back contact interphase due to a favorable band alignment with CuBi<sub>2</sub>O<sub>4</sub>.<sup>[207]</sup>

In other heterojunctions, both components are narrow bandgap semiconductors. In this regard, heterojunctions of CuBi<sub>2</sub>O<sub>4</sub> with CuO have been extensively studied,<sup>[92,108,208–211]</sup> FTO/CuO/CuBi<sub>2</sub>O<sub>4</sub> electrodes double the photoactivity of the homolayered electrode (after Pt loading in all cases),<sup>[208]</sup> which is explained based on enhanced electron–hole separation because of the valence band offset existing at the solid–solid interface. In fact, when the heterojunction is inverted, the photocurrent decreases because of a promotion of electron–hole recombination. Nanocomposites of CuBi<sub>2</sub>O<sub>4</sub> with CuO (and with Bi<sub>2</sub>O<sub>3</sub>) have also been generated in situ by changing the Cu:Bi ratio in the precursor solution.<sup>[92,209]</sup> Moreover, heterojunctions can be formed by a heat treatment that induces a partial reaction of the ternary oxide to generate a binary oxide. For instance, an oxidative heat treatment of Cu<sub>3</sub>VO<sub>4</sub><sup>[169]</sup> generates CuO at the surface, together with an oxygen excess in the structure (metal deficiency), leading to an increase in the photoresponse. Along the same lines, Sullivan et al.<sup>[164]</sup> identified the formation of a TMO/CuO junction in Cu<sub>5–x</sub>Ta<sub>11</sub>O<sub>30</sub> electrodes after a heat treatment between 250 and 550 °C. The generated CuO islands provide a favorable band offset with the TMOs, thus improving charge separation.

### 3.3. Improving Charge Collection through Doping

Doping is a critical strategy for the achievement of high efficiencies in TMO photocathodes, as they usually suffer from poor charge carrier transport (see Section 2). Consequently, there is a significant number of reports dealing with this strategy including not only increasing the conductivity but also switching the conductivity type (p or n).

#### 3.3.1. Doping Induced by a Third Metal

The intentional introduction of impurity atoms in the semiconductor lattice is the typical strategy used to produce a doping effect. In TMOs, a third metal is incorporated into the oxide lattice, having an ionic radius similar to that of one of the intrinsic metals, while its oxidation state is different. This induces new impurity levels that may increase the density of majority carriers, enhancing thus the conductivity of the bulk material. The mobility of charge carriers may also be affected by doping because

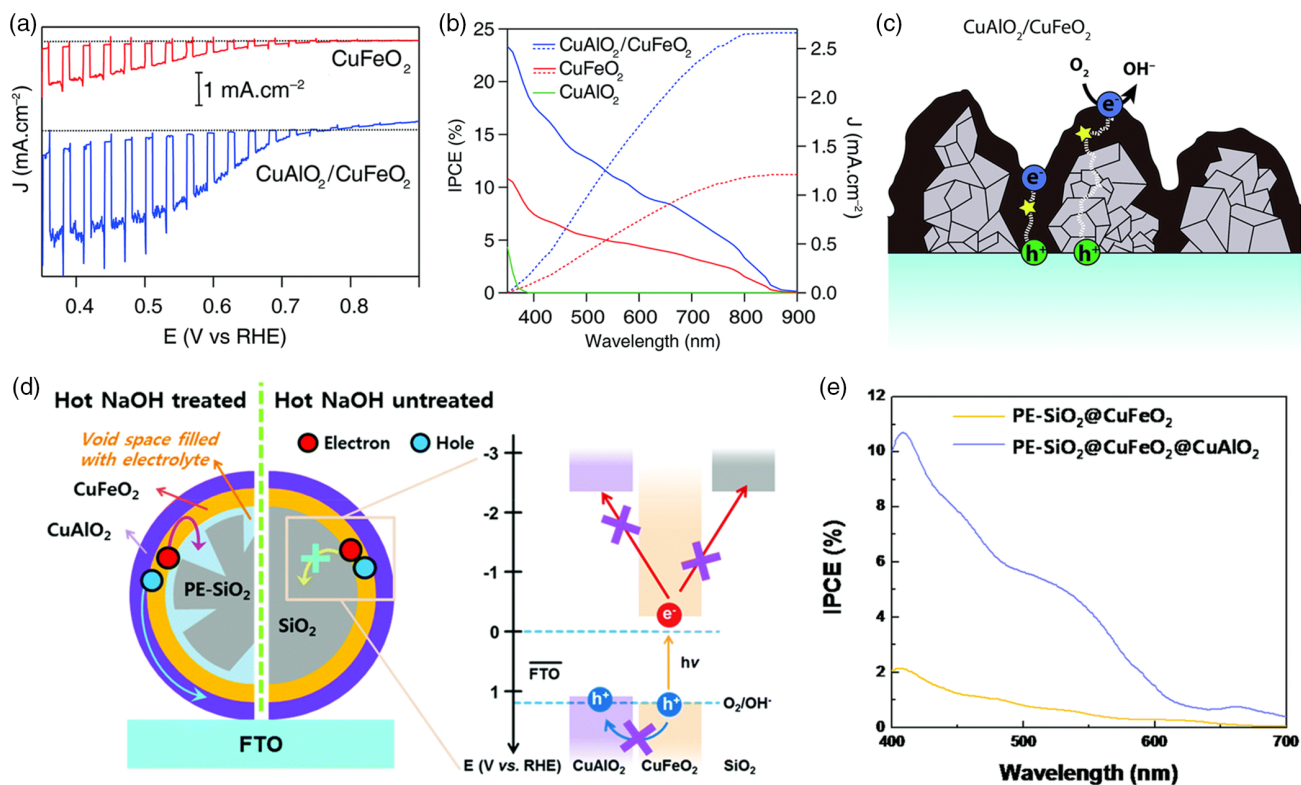


**Figure 9.** a) Linear sweep voltammograms for  $\text{CuFeO}_2$  (red line) and  $\text{CuAlO}_2/\text{CuFeO}_2$  (blue line) electrodes under transient 1 sun illumination in 1 M NaOH under  $\text{O}_2$  bubbling (scan rate of  $10 \text{ mV s}^{-1}$ ) and b) IPCE for  $\text{CuFeO}_2$ ,  $\text{CuAlO}_2$ , and  $\text{CuAlO}_2/\text{CuFeO}_2$  (solid lines) and the corresponding integrated photocurrents (dotted lines). c) Scheme showing the possible path for photogenerated charge carriers in the  $\text{CuAlO}_2/\text{CuFeO}_2$  photoelectrode. Reproduced with permission.<sup>[206]</sup> Copyright 2016, The Royal Society of Chemistry. d) Illustration of a silica microsphere partially etched by hot NaOH treatment at the left and that of an untreated one at the right. Scheme of the energy band diagram showing the electron transfer pathways at the  $\text{CuFeO}_2/\text{electrolyte}$  interface. e) IPCE spectra for a  $\text{CuFeO}_2$ -shelled microsphere electrode with and without the outer  $\text{CuAlO}_2$  layer in  $\text{O}_2$ -purged 1 M NaOH at 0.6 V versus RHE. Reproduced with permission.<sup>[119]</sup> Copyright 2018, The Royal Society of Chemistry.

of the structural changes generated in the lattice. In the case of p-type oxide semiconductors, the doping metal should have an oxidation state lower than that of the intrinsic metal as to create electron acceptor impurities and enhance the p-type character.

In 1988, Matsumoto et al.<sup>[212]</sup> were the first to show an improvement of the photocurrent of a TMO photocathode through doping with metals. They reported that  $\text{Fe}^{4+}$  was created upon doping of  $\text{CaFe}_2\text{O}_4$  with  $\text{Mg}^{2+}$  and  $\text{Na}^+$ . The  $\text{Fe}^{4+}$  species acts as an acceptor that generates a hole in the valence band according to  $\text{Fe}^{4+} \rightarrow \text{Fe}^{3+} + h_{\text{VB}}^+$ . The increase in hole density enhances the material conductivity. Another effect reported in that work is that doping near the  $\text{CaFe}_2\text{O}_4/\text{metal}$  interface gives rise to the formation of an ohmic contact, which also contributes to the improvement of the photoresponse. More recently, doping  $\text{LaFeO}_3$  with divalent ions has been widely studied since Díez-García and Gómez<sup>[139]</sup> showed that partial substitution of  $\text{Fe}^{3+}$  by  $\text{Mg}^{2+}$  or  $\text{Zn}^{2+}$  in  $\text{LaFeO}_3$  photocathodes yielded a dramatic increase of the photocurrents in the presence of oxygen. In that case, Mg and Zn salts were directly introduced in the sol-gel precursor solution. An increase of the charge carrier density was uncovered by the analysis of the Mott-Schottky plots and a positive effect on the charge carrier mobility was also suggested. Following the same preparative routes for synthesis and

modification, Quiñonero et al.<sup>[142]</sup> were able to prepare  $\text{NdFeO}_3$  photocathodes and to dope them with Mg and Zn. The photoelectrochemical behavior of the undoped and doped materials was similar to that of  $\text{LaFeO}_3$ . A DFT study pointed to the fact that the enhanced p-type character induced by doping is due to an increase of the hole density rather than to an effect on charge mobility. In addition, an increase of the p-type character upon doping can be understood by both the appearance of empty states above the valence band and the flattening of the bands in the CB, which is indicative of an increase in the electron effective mass. Another work by Sun et al.<sup>[213]</sup> focused on the effect of doping with divalent alkaline-earth metal cations (Mg, Ca, Sr, and Ba) in  $\text{LaFeO}_3$  prepared by sol-gel. The authors claimed that the increase in the photocurrent is linked to the attenuation of states located around 100–200 meV above the valence band edge that are linked to intrinsic defects (cation vacancies) and act as hole-traps. An increase of the majority carrier density was reported upon K and Li<sup>[180]</sup> doping of  $\text{LaFeO}_3$ . Weeler et al.<sup>[179]</sup> attributed this effect to the introduction of shallow acceptor levels above the valence band maximum induced by the substitutional doping with K. In this case, the perovskite was synthesized by electrodeposition, and K was introduced in the lattice by drop casting a solution of a potassium salt with

a subsequent heat treatment. K and Li doping can also decrease the bandgap by lowering the conduction band minimum (see Section 3.1.1). Interestingly, theoretical work reveals that the two holes generated by the substitution of a La ion by a K ion are localized at an iron and at one of its neighboring O atoms, leading to the presence of  $\text{Fe}^{4+}$ . The  $\text{Fe}^{4+}$  density was monitored by XPS, changing from 7.7 at% (respect to the total amount of Fe) for the bare material to a 15.9 at% with a 3 at% K-doped  $\text{LaFeO}_3$ . As a general trend in these works, in the absence of an electron scavenger ( $\text{O}_2$ ), although the photocurrent spikes increase in the doped samples due to the improved conductivity, the stationary photocurrents remain very low for water reduction, indicating that electron transfer to water from  $\text{LaFeO}_3$  is still challenging even after doping.

Similarly to  $\text{LaFeO}_3$ , Jiang et al.<sup>[120]</sup> have reported that doping  $\text{CuFeO}_2$  with  $\text{Mg}^{2+}$ , using a hydrothermal bath synthesis, produces an increase in the majority carrier concentration and an enhanced lifetime of the photogenerated charge carriers. Ni doping has also been reported in the case of  $\text{CuFeO}_2$  delafossite.<sup>[214]</sup> Regarding other TMOs, Kang et al.<sup>[93]</sup> introduced Ag in  $\text{CuBi}_2\text{O}_4$ .  $\text{Ag}^+$  replaced  $\text{Bi}^{3+}$  ions in the structure and increased hole concentration. In addition to the positive impact on the photoresponse (in the presence of  $\text{O}_2$ ), photocorrosion of  $\text{CuBi}_2\text{O}_4$  was also suppressed.

The creation of acceptor impurities can even change the n-type character to p-type as stated before. A representative example is the doping of n-type  $\text{SrTiO}_3$  with Rh (already mentioned in Section 3.1.1).<sup>[177]</sup> The Rh-doped photoelectrodes present photocathodic behavior with optimum performance for Rh/(Ti+Rh) 7 at% Rh. Later, Kawasaki et al.<sup>[178]</sup> also studied Rh-doped  $\text{SrTiO}_3$  forming epitaxial thin films fabricated by PLD. The oxygen pressure and temperature selected during film growth were found to affect the oxidation state of the Rh dopant (either  $\text{Rh}^{4+}$  or  $\text{Rh}^{3+}$ ). In the material containing  $\text{Rh}^{4+}$ , the photocurrent onset was shifted 0.6 V toward less positive potentials with respect to the material containing  $\text{Rh}^{3+}$ . Very recently, Lan et al.<sup>[88]</sup> studied a p-type Co-doped  $\text{ZnFe}_2\text{O}_4$  with 1D rod-like morphology via hydrothermal synthesis. They demonstrated that the material could sustain overall water splitting. The bare  $\text{ZnFe}_2\text{O}_4$  electrodes display n-type behavior based on a Mott-Schottky analysis. Together with a decrease of the bandgap (see Section 3.3.1), the cobalt doping produced a tuning from n- to p-type character, leading to a 7.33-fold increase of the photocathodic currents.

Apart from the effect on the acceptor impurities, conductivity can also be improved by attaining higher carrier mobility. Sekizawa et al.<sup>[215]</sup> reported that Ag doping in  $\text{CaFe}_2\text{O}_4$  triggered an improvement in the symmetry around the Fe atom, which induces high mobility (higher diffusion length of the charge carriers), considered the main reason for the 23-fold increase in the cathodic photocurrent.

### 3.3.2. Doping Induced by Oxygen Intercalation

Another approach that can promote doping is the increase in the oxidation state of some metal atoms in the lattice triggered by the incorporation of interstitial oxygen. Such an effect is usually

achieved through heat treatments in oxidizing atmospheres or particular synthetic conditions (including electrosynthesis).

Enhancing the p-type character by an oxidative treatment has been carried out by heating the material in an  $\text{O}_2$ -rich atmosphere, typically air. This leads to oxygen excess in the structure, generally linked to an increase in charge carrier density. The Maggard group has extensively applied this method to improve the photoactivity of many TMOs.<sup>[136,163,164,169,181]</sup> In this way,  $\text{CuNbO}_3$  electrodes, after a mild oxidation treatment at 250 °C in air, have been shown to exhibit a positive shift of the onset potential.<sup>[136]</sup> Subsequent work<sup>[181]</sup> revealed that Cu deficiency was generated owing to the formation of  $\text{CuO}$  at the surface, leading to a stoichiometry  $\text{Cu}_{0.984}\text{NbO}_3$ . Similarly, an oxidation treatment at 250–550 °C in air of  $\text{Cu}_5\text{Ta}_{11}\text{O}_{30}$  and  $\text{Cu}_3\text{Ta}_7\text{O}_{19}$  materials<sup>[163]</sup> also produced a notable increase in the cathodic photocurrents. In the  $\text{Cu}_5\text{Ta}_{11}\text{O}_{30}$  case, the enhancement was primarily attributed to acceptor densities 4 orders of magnitude larger in the case of the oxidized samples. Later, a more detailed study of the temperature and duration of the oxidation treatment was performed for  $\text{Cu}_5\text{Ta}_{11}\text{O}_{30}$  electrodes.<sup>[164]</sup> In this case, the largest increase of the photocurrents was observed for a temperature of 350 °C, which was correlated with maximum changes in the amount of Cu vacancies because of the formation of  $\text{CuO}$  surface islands, which, in turn, improved electron-hole separation (as commented in the preceding section). More recently, a  $\text{CuFeO}_2$  photocathode was also submitted to an oxidation treatment at 300 °C and again, an increase in carrier density (detected by a Mott-Schottky analysis) was linked to the improved photoactivity.<sup>[114]</sup> Later, Lee and co-workers<sup>[216]</sup> devised that a hybrid microwave annealing (HMA) was more effective for  $\text{CuFeO}_2$  electrodes than the conventional one in a furnace (**Figure 10a**). They observed a higher and more homogenous distribution of  $\text{Cu}^{2+}$  in the film due to a more efficient oxygen intercalation with the HMA treatment, increasing the acceptor density (**Figure 10b**). More recently, Park and co-workers<sup>[217]</sup> have developed a flame-annealing synthesis method for  $\text{CuFe}_2\text{O}_4$  on FTO consisting in applying a high temperature (<980 °C) for a short time. Importantly, the procedure avoids significant damage to the FTO. As a result, IPCE values up to 30% are achieved, not only because of a reduction of the oxygen vacancy density, but also because of a higher surface area and improved optical absorption compared with the material resulting from an ordinary furnace treatment. The flame annealing allows for a rapid heating and cooling rate of the samples while providing an  $\text{O}_2$ -rich atmosphere.

Besides by heat treatment, the increase of the acceptor density can also be achieved through an electrochemical treatment. Such a strategy has been investigated previously not only for  $\text{TiO}_2$ ,<sup>[218]</sup> but also for  $\text{NiTiO}_3$ <sup>[219]</sup> photoanodes, in which a reductive pretreatment induces an increase of the catalytic activity for water oxidation. An analogous behavior has been observed by Díez-García et al.<sup>[87]</sup> in the case of  $\text{CuFe}_2\text{O}_4$  photocathodes by applying a potentiodynamic oxidative treatment. They observed an enhancement of the p-type character revealed by both an increase of the currents associated with the charge accumulation region (**Figure 10c**) and higher photocathodic currents (**Figure 10d**). This effect was tentatively ascribed to the formation of  $\text{CuFe}_2\text{O}_{4+x}$ , together with an increase of the acceptor density.



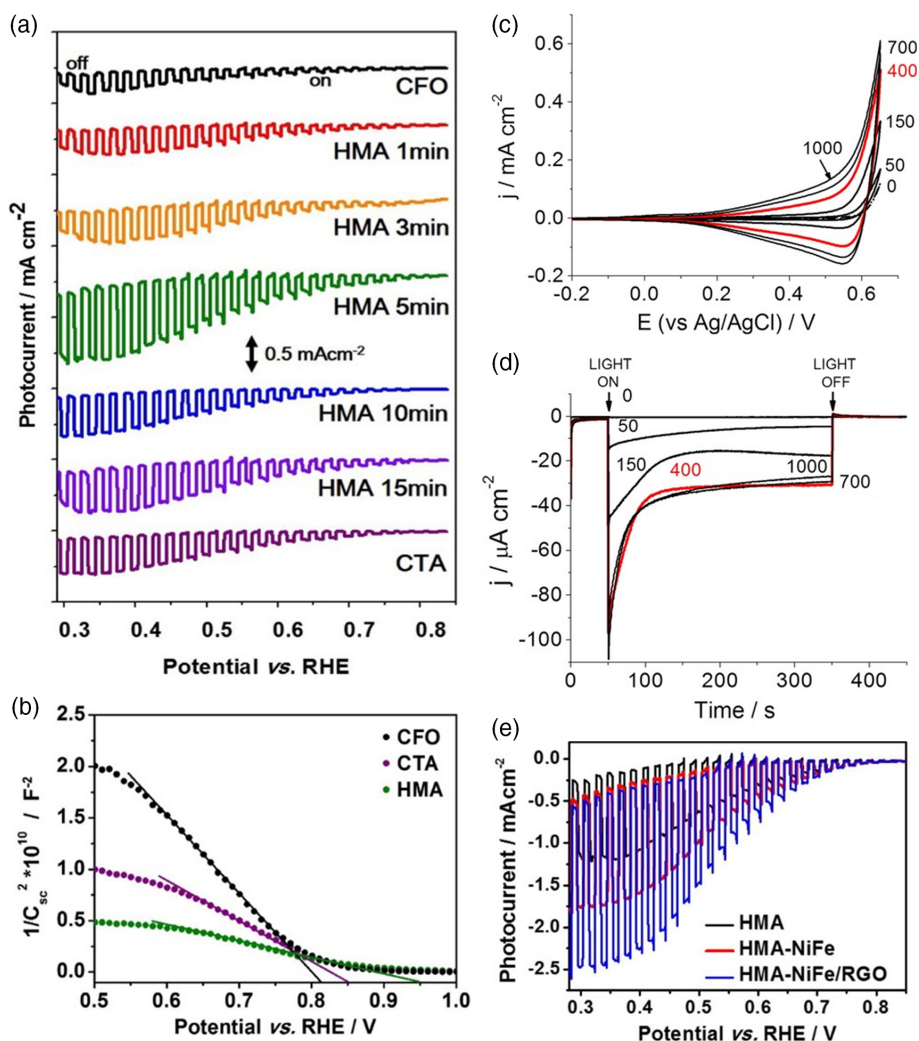


**Figure 10.** a) Linear sweep voltammograms under transient illumination for untreated  $\text{CuFe}_2\text{O}_4$  (CFO), after conventional thermal annealing at  $300^\circ\text{C}$  (CTA) and after hybrid microwave annealing (HMA) for different treatment durations and b) Mott-Schottky plots for CFO, CTA, and HMA electrodes in Ar-purged 1 M NaOH. Reproduced with permission.<sup>[216]</sup> Copyright 2016, American Chemical Society. c) Cyclic voltammograms in the dark after different numbers of cycles between  $-0.2$  and  $0.65$  V at  $500$   $\text{mV s}^{-1}$  (scan rate of  $20$   $\text{mV s}^{-1}$ ) and d) photocurrent transients at  $-0.2$  V for a  $\text{CuFe}_2\text{O}_4$  electrode after the indicated number of voltammetric cycles in  $\text{N}_2$ -purged  $0.1$  M NaOH. Reproduced with permission.<sup>[87]</sup> Copyright 2016, Wiley-VCH. e) Linear sweep voltammogram under 1 sun transient illumination for hybrid microwave annealed  $\text{CuFe}_2\text{O}_4$  electrode, after depositing NiFe and NiFe/RGO cocatalysts in Ar-purged 1 M NaOH. Reproduced with permission.<sup>[216]</sup> Copyright 2016, American Chemical Society.

Berglund and co-workers<sup>[220]</sup> developed another novel and successful strategy based on a self-doping of  $\text{CuBi}_2\text{O}_4$  synthesized by spray pyrolysis. A concentration gradient of copper across the film generates a gradient of copper vacancies that act as acceptor dopants. This induces the generation of an electric field that helps to separate the charge carriers within the material.

### 3.4. Improving Interfacial Reaction Kinetics by Cocatalysts

Incorporating a cocatalyst on the absorber material is an almost indispensable step in designing highly efficient photoelectrodes. Even if the photogenerated electrons and holes possess appropriate potentials for driving water splitting reactions, the photocatalytic activity may still be low. This can be due not only to surface recombination facilitated by the presence of surface

states, but also to the existence of a low density of active sites and/or to a sluggish charge transfer kinetics from them. A surface-loaded cocatalyst is needed to facilitate the transfer of minority carriers through the semiconductor/electrolyte interface as it reduces the energy barrier for the electrochemical process. Transition metals, especially noble metals, are traditionally used as effective electrocatalysts for  $\text{H}_2$  evolution. These metals act as electron sinks and provide effective proton reduction sites.<sup>[221]</sup>

Platinum metal is an exceedingly good electrocatalyst for the HER and it has been demonstrated to be effective as a cocatalyst with the most common photocathode materials, such as  $\text{Cu}_2\text{O}$ <sup>[59,222,223]</sup> and  $\text{Si}$ .<sup>[224,225]</sup> Regarding TMOs, Pt was deposited electrochemically on  $\text{CaFe}_2\text{O}_4$  and  $\text{Sr}_7\text{Fe}_{10}\text{O}_{22}$  surfaces, leading to larger photocurrents due to the acceleration of the kinetics of

H<sub>2</sub> evolution and the inhibition of surface recombination.<sup>[77]</sup> Pt was also successfully coated on CuBi<sub>2</sub>O<sub>4</sub> photocathodes increasing the cathodic photocurrents.<sup>[93,94,104,208]</sup> In the work of Berglund et al.,<sup>[94]</sup> IPCE values increased from about 3% for the bare material to 20% at 300 nm when Pt was loaded on CuBi<sub>2</sub>O<sub>4</sub>.

In some cases, direct deposition of the cocatalyst on the p-type material does not produce the expected effect. This is because not only its catalytic properties are important, but also a proper junction between the semiconductor and the cocatalyst. In such cases, engineering of the interphase is needed, and the most common approach is the deposition of intermediate (buffer) layers between the semiconductor and the cocatalyst, for which TiO<sub>2</sub> is typically employed.<sup>[60,114,161,226]</sup> In the work of Prévot et al.<sup>[114]</sup> direct loading of the catalyst at the CuFeO<sub>2</sub> surface led to inconsistent results. Following the method of Tilley et al. for Cu<sub>2</sub>O electrodes,<sup>[60]</sup> they achieved an improved photoresponse with CuFeO<sub>2</sub>/AZO/TiO<sub>2</sub>/Pt electrodes for water reduction with respect to the bare TMO electrode, with the drawback of shifting the onset potential toward more negative values. In agreement with these findings, Shen et al.<sup>[161]</sup> revealed that the direct deposition of Pt on BiFeO<sub>3</sub> electrodes leads to a decrease of the photocurrent. On the contrary, the indium tin oxide (ITO)/BiFeO<sub>3</sub>/TiO<sub>2</sub>/Pt configuration dramatically increased the photocurrents and shifted the onset potential toward positive values with respect to the bare perovskite electrode. The TiO<sub>2</sub> deposit acts as a buffer layer, removing the upward barrier generated by the direct contact of the semiconductor and Pt. A similar effect was observed using a carbon porous layer instead of TiO<sub>2</sub>.<sup>[160]</sup>

It should be stressed that there is a need for the exploration of new cocatalysts that are more cost-effective than Pt. Nickel-based materials (Ni,<sup>[227–229]</sup> Ni–Mo,<sup>[230]</sup> NiO<sub>x</sub>,<sup>[231]</sup> and Ni(OH)<sub>2</sub><sup>[229]</sup>), and MoS<sub>2+x</sub><sup>[230]</sup> have been tested successfully for Cu<sub>2</sub>O, but to the best of our knowledge, no reports refer their use for p-type TMOs. However, a few recent studies focused on the use of cost-effective cocatalyst for PEC HER based on NiFe and CoFe double layered hydroxides (DLH) previously tested for other semiconductors.<sup>[232]</sup> Recently, Jan et al.<sup>[216]</sup> have incorporated NiFe DLH on CuFeO<sub>2</sub>, enhancing the HER activity (Figure 10e). Further improvement has been achieved by the combination of NiFe with reduced graphene oxide. Similarly, a C<sub>60</sub>/CoFe DLH cocatalyst enhanced photocurrents by a factor of 4.6 for a CuFeO<sub>2</sub> inverse opal nanostructured electrode (Figure 7g). C<sub>60</sub> was deposited simply by drop casting while CoFe DLH nano-sheets were uniformly electrodeposited over CuFeO<sub>2</sub>/C<sub>60</sub>.<sup>[121]</sup> In both works, the photoresponse of the CuFeO<sub>2</sub>-based photocathodes outperformed that reported in the literature.

## 4. Conclusions

In the last years, the development of photocathodes based on ternary metal oxides that could outperform the few existing p-type binary oxides has been boosted by the need of finding new materials for efficient and stable water-splitting PEC cells. In the same way, different strategies have been applied to optimize the behavior of these materials, most of them based on the knowledge gained in the study of, among others, binary metal

oxides. Apart from an experimental approach, theoretical methods are gaining relevance and DFT studies are helping to get insights into the band structure and the effect of the introduction of dopants, thus contributing to the understanding and prediction of the photoelectrochemical properties of new materials. This is an appropriate research direction as the knowledge of the mechanisms for photoelectrochemical water reduction are only partially understood, which, in turn, hinders an a priori design of enhancement strategies.

Most of the reported ternary metal oxides showing a p-type behavior are spinels, although studies on delafossites, perovskites, and other oxides with more complex stoichiometries (i.e., such as those of vanadates, niobates and tantalates) are gaining importance. In this context, Fe-containing materials are the most studied, probably because of the earth-abundance, cost-effectiveness, and environmental friendliness of Fe. The possibility of generating p-type ternary oxides based on Fe is directly related to the feasibility of forming Fe<sup>4+</sup> in the crystalline structure, which has been reported as responsible for their p-type character. In addition, most Fe-based perovskites and spinels can also present n-type character depending on the synthetic procedure, which determines the type of prevailing defects. Other attractive features of Fe-based oxides are their relatively narrow bandgaps (1.5–2.7 eV) and their demonstrated stability under illumination and cathodic conditions, which is a major advantage over most of the Cu-based materials. Conversely, Fe-based materials such as CaFe<sub>2</sub>O<sub>4</sub>, CuFeO<sub>2</sub>, and LaFeO<sub>3</sub> suffer from poor conductivity. In this regard, doping with monovalent and divalent cations, such as alkaline metals or zinc ions have been extensively studied in the last years. The reported results demonstrate that this is a general and effective strategy for increasing the charge carrier density, thus enhancing the p-type character. However, these materials (CuFeO<sub>2</sub> and Fe-perovskites) are reported to yield extremely low photocurrents ascribed to hydrogen production, which dramatically increase in the presence of oxygen as an electron scavenger. In this regard, some studies on CuFeO<sub>2</sub> and CaFe<sub>2</sub>O<sub>4</sub> have revealed that Fermi level pinning governs the interface between the semiconductor and the electrolyte, hindering charge transfer to water. To overcome this limitation recent efforts have focused on the deposition of cocatalysts together with intermediate buffer layers.

Apart from the Fe-containing oxides, Cu-containing materials have also been extensively studied. Specifically, copper vanadates, niobates and tantalates having different stoichiometries have been investigated as most of them present narrow bandgaps. Heat treatments of these compounds generally lead to improved photoresponses because the oxidation of copper can produce an increase of the charge carrier density and/or a favorable heterojunction with CuO generated by direct oxidation of the ternary oxide. CuBi<sub>2</sub>O<sub>4</sub> has attracted a lot of attention in the last years because it displays high photocurrents for water photoreduction at moderate potentials (0.4–0.6 V vs RHE), having a relatively narrow bandgap (1.5–1.8 eV). For this material, a heterojunction with CuO seems to be a viable strategy for enhancing charge separation and increasing photocurrents, while stability has been improved by the deposition of protective TiO<sub>2</sub> layers. Although typically Cu-based TMOs are more stable than copper binary oxides, they still need to be improved using proper protection strategies. Finally, Rh-containing ternary metal oxides,

$\text{CuRhO}_2$  and  $\text{CuRh}_2\text{O}_4$ , are reported to yield high IPCE values (higher than 15% at 400 nm), among the best for ternary metal oxides without any further modification, and good stability. However, Rh is a scarce and expensive metal that hinders the practical application of Rh oxides.

Despite the number of TMOs reported in photoelectrochemical studies, in our opinion there is still room for discovering new complex semiconductor oxides that could be efficient as photocathodes. However, it should be mentioned that some of them remain unexplored as photoelectrodes because high temperatures are needed for pure phase formation, limiting the direct growth on the typical transparent conductive substrates and, more generally, reducing their technical viability. In some cases, the deposition of presynthesized nano/microparticles suffers from defective interparticle connection, leading to poor charge carrier transport. In the arduous task of finding new oxides, the use of the principles of combinatorial chemistry will be critical, including the theoretical screening of potential candidates. In this respect, computational chemistry methods, such as DFT will be of particular importance.

The development and optimization of enhancement strategies are imperative for approaching maximum theoretical solar efficiency and providing long-term stability. Doping has been demonstrated to be effective for increasing the photocurrents for hydrogen evolution by the improvement of charge transport through the material. Heterojunctions with proper band alignments have also demonstrated to improve charge separation.

An important challenge to face is the sluggish electron transfer from the semiconductor surface to water. This has been improved in some materials by direct loading of cocatalysts, mainly Pt. For ternary metal oxides, studies on Earth-abundant cocatalysts are relatively scarcer. Remarkably, CoFe and NiFe hydroxides have led to excellent results in alkaline media. However, for other materials, issues have been reported when loading a metal cocatalyst, pointing to the need of an intermediate buffer layer to observe a noticeable catalytic effect. The development of a proper surface engineering for the effective loading of cocatalysts is a key aspect for improving both the photoresponse and the stability of the photocathodes. Another important limitation in the electron transfer to water is the presence of surface states. In some cases, passivation of these states is imperative for improving electron transfer to the electrolyte. This has been achieved by the deposition of very thin layers over the absorber material, usually by means of sophisticated techniques such as ALD or PLD, which are difficult to scale up. The deposition of p–n junctions is not as restrictive concerning thickness and homogeneity of the layer as that of passivation layers, and they can also suppress the effect of the surface states as the initial absorber-electrolyte interface is substituted by the new absorber-junction material-electrolyte interfaces. On the other hand, the formation of 1D structures is also thought to be a promising route to enhance the PEC performance by alleviation of slow carrier mobilities. In this regard, there is a lack of procedures for the formation of ordered nanostructures in ternary oxide photocathodes, which is a field to explore.

Up to now,  $\text{CuBi}_2\text{O}_4$ ,  $\text{CuFeO}_2$ , and  $\text{LaFeO}_3$  are the ternary oxides most studied as photocathodes for the HER. Probably,  $\text{CuBi}_2\text{O}_4$  is closer to find practical application in tandem cells with reported IPCE values higher than 10% for the bare material

and around 30% after application of some enhancement strategies. The viability of bias free cells when combined with photoanodes having a wider bandgap has been demonstrated, although application of bias probably will be required for reaching high solar conversion efficiencies. However, suitable protective strategies should be identified to address the stability issue. In addition, the interface architecture involving the cocatalyst together with buffer layers should be optimized as significantly higher photocurrents are reported using  $\text{H}_2\text{O}_2$  as an electron scavenger. In the case of Fe-based perovskites and delafossites, hole collection has been improved by doping and by applying scaffold layers. The major challenge in these materials is the hindered electron transfer to water. In this respect, some recent works have uncovered major improvements of the  $\text{CuFeO}_2$  efficiency by using metal hydroxide cocatalysts. Finally, in the case of  $\text{LaFeO}_3$ , most of the measurements are carried out in the presence of  $\text{O}_2$  and efforts should focus on surface engineering to increase the low photocurrents for water reduction reported up to now.

We believe that this review demonstrates that ternary metal oxides can be adequate candidates as photocathodes for water splitting tandem cells. However, the practical implementation of these materials is limited due to: (i) the high cost of reagents or complex (or non-scalable) synthetic routes, (ii) low (faradaic) efficiencies for hydrogen evolution, or (iii) poor stability for long-time illumination.

Based on the current state of the art, it seems apparent that, to achieve highly efficient and stable ternary metal oxide materials, efforts should follow the following directions (i) improving the photoresponse and stability of the currently known, most promising candidates for a practical device (made from Earth-abundant elements and cost-effective materials and synthetic routes) by using different modification strategies. ii) Gaining a deeper understanding of the photocathode processes leading to hydrogen evolution to define the modification strategies to be implemented. (iii) Identifying suitable methodologies for guiding the search for complex multinary materials on rational bases, i.e., DFT calculations. We believe that high solar efficiencies in ternary metal oxide photocathodes can only be reached with appropriate electrode engineering using a smart combination of strategies including doping, heterojunctions and surface layers, and cocatalysts, to minimize charge recombination.

Currently, there is a world-wide, renewed interest in the development of hydrogen as an energy vector, and more specifically in solar (green) hydrogen. Photoelectrochemical water splitting is one of the emerging technologies that deserves further attention. Finding adequate electrode materials keeps on being a critical step, being transition metal oxides appropriate candidates as they could, in principle, possess higher stability than other metal compounds. We think that this review may contribute to guide future research in the selection and optimization of oxides for photoelectrochemical water splitting.

## Acknowledgements

The authors gratefully acknowledge funding from the European Union's Horizon 2020 research and innovation programme under grant agreement no. 760930 (FotoH2 project).

## Conflict of Interest

The authors declare no conflict of interest.

## Keywords

artificial photosynthesis, doping, overlayers, photoelectrochemical cells, p-type semiconductor materials, solar hydrogen production, underlayers, water splitting

Received: October 18, 2021

Revised: December 6, 2021

Published online: January 14, 2022

- [1] R. van de Krol, M. Grätzel, in *Photoelectrochemical Hydrogen Production* (Eds: R. van de Krol, M. Grätzel), Springer Science+Business Media, LLC, New York, NY, USA **2012**.
- [2] N. S. Lewis, G. Crabtree, *Report on Basic Energy Sciences Workshop on Solar Energy Utilization*, U.S. Department Of Energy, Washington, DC, USA, **2005**.
- [3] F. E. Osterloh, *Chem. Soc. Rev.* **2013**, *42*, 2294.
- [4] N. S. Lewis, *Science* **2016**, *351*, aad1920.
- [5] L. M. Peter, *Electroanalysis* **2015**, *27*, 864.
- [6] M. Grätzel, *Nature* **2001**, *414*, 338.
- [7] K. Sivula, M. Grätzel, in *Photoelectrochemical Water Splitting: Materials, Processes and Architectures* (Eds: H. Lewerenz, L. Peter), RSC Publishing, Cambridge, UK **2013**.
- [8] M. G. Walter, E. L. Warren, J. R. McKone, S. W. Boettcher, Q. Mi, E. A. Santori, N. S. Lewis, *Chem. Rev.* **2010**, *110*, 6446.
- [9] M. C. Hanna, A. J. Nozic, *J. Appl. Phys.* **2006**, *100*, 074510.
- [10] B. A. Pinaud, J. D. Benck, L. C. Seitz, A. J. Forman, Z. Chen, T. G. Deutsch, B. D. James, K. N. Baum, G. N. Baum, S. Ardo, H. Wang, E. Miller, T. F. Jaramillo, *Energy Environ. Sci.* **2013**, *6*, 1983.
- [11] A. Fujishima, K. Honda, *Nature* **1972**, *238*, 37.
- [12] M. Ni, M. K. H. Leung, D. Y. C. Leung, K. Sumathy, *Renewable Sustainable Energy Rev.* **2007**, *11*, 401.
- [13] Y. Lin, G. Yuan, R. Liu, S. Zhou, S. W. Sheehan, D. Wang, *Chem. Phys. Lett.* **2011**, *507*, 209.
- [14] T. Berger, D. Monllor-Satoca, M. Jankulovska, T. Lana-Villarreal, R. Gómez, *ChemPhysChem* **2012**, *13*, 2824.
- [15] K. Sivula, F. Le Formal, M. Grätzel, *ChemSusChem* **2011**, *4*, 432.
- [16] Y. Qiu, S.-F. Leung, Q. Zhang, B. Hua, Q. Lin, Z. Wei, K. Tsui, Y. Zhang, S. Yang, Z. Fan, *Nano Lett.* **2014**, *14*, 2123.
- [17] P. Tang, H. Xie, C. Ros, L. Han, M. Biset-Peiró, Y. He, W. Kramer, A. Pérez Rodríguez, E. Saucedo, J. R. Galán-Mascarós, T. Andreu, J. R. Morante, J. Arbiol, A. P. Rodríguez, E. Saucedo, J. R. Galán-Mascarós, T. Andreu, J. R. Morante, J. Arbiol, *Energy Environ. Sci.* **2017**, *10*, 2124.
- [18] G. Carraro, C. Maccato, A. Gasparotto, M. E. A. Warwick, C. Sada, S. Turner, A. Bazzo, T. Andreu, O. Pliekhova, D. Korte, U. Lavrenčič Štangar, G. Van Tendeloo, J. R. Morante, D. Barreca, *Sol. Energy Mater. Sol. Cells* **2017**, *159*, 456.
- [19] V. Cristino, S. Caramori, R. Argazzi, L. Meda, G. L. Marra, C. A. Bignozzi, *Langmuir* **2011**, *27*, 7276.
- [20] J. Zhao, E. Olide, F. E. Osterloh, *J. Electrochem. Soc.* **2014**, *162*, H65.
- [21] C. Fàbrega, S. Murcia-López, D. Monllor-Satoca, J. D. Prades, M. D. Hernández-Alonso, G. Penelas, J. R. Morante, T. Andreu, *Appl. Catal. B Environ.* **2016**, *189*, 133.
- [22] I. Fujimoto, N. Wang, R. Saito, Y. Miseki, T. Gunji, K. Sayama, *Int. J. Hydrogen Energy* **2014**, *39*, 2454.
- [23] L. Zhang, C. Y. Lin, V. K. Valev, E. Reisner, U. Steiner, J. J. Baumberg, *Small* **2014**, *10*, 3970.
- [24] J. Quiñero, T. Lana-Villarreal, R. Gómez, *Appl. Catal. B Environ.* **2016**, *194*, 141.
- [25] S. Murcia-López, C. Fàbrega, D. Monllor-Satoca, M. D. Hernández-Alonso, G. Penelas-Pérez, A. Morata, J. R. Morante, T. Andreu, *ACS Appl. Mater. Interfaces* **2016**, *8*, 4076.
- [26] D. K. Lee, K. S. Choi, *Nat. Energy* **2018**, *3*, 53.
- [27] L. Gao, Y. Cui, J. Wang, A. Cavalli, A. Standing, T. T. T. Vu, M. A. Verheijen, J. E. M. Haverkort, E. P. A. M. Bakkers, P. H. L. Notten, *Nano Lett.* **2014**, *14*, 3715.
- [28] Y. Lin, R. Kapadia, J. Yang, M. Zheng, K. Chen, M. Hettick, X. Yin, C. Battaglia, I. D. Sharp, J. W. Ager, A. Javey, *J. Phys. Chem. C* **2015**, *119*, 2308.
- [29] L. Gao, Y. Cui, R. H. J. Vervuurt, D. Van Dam, R. P. J. Van Veldhoven, J. P. Hofmann, A. A. Bol, J. E. M. Haverkort, P. H. L. Notten, E. P. A. M. Bakkers, E. J. M. Hensen, *Adv. Funct. Mater.* **2016**, *26*, 679.
- [30] A. B. Bocarsly, D. C. Bookbinder, R. N. Dominey, N. S. Lewis, M. S. Wrighton, *J. Am. Chem. Soc.* **1980**, *102*, 3683.
- [31] U. Sim, H.-Y. Jeong, T.-Y. Yang, K. T. Nam, *J. Mater. Chem. A* **2013**, *1*, 5414.
- [32] R. H. Coridan, M. Shaner, C. Wiggenhorn, B. S. Brunschwig, N. S. Lewis, *J. Phys. Chem. C* **2013**, *117*, 6949.
- [33] S. Huang, H. Zhang, Z. Wu, D. Kong, D. Lin, Y. Fan, X. Yang, Z. Zhong, S. Huang, Z. Jiang, C. Cheng, *ACS Appl. Mater. Interfaces* **2014**, *6*, 12111.
- [34] C. Ros, T. Andreu, M. D. Hernández-Alonso, G. Penelas-Pérez, J. Arbiol, J. R. Morante, *ACS Appl. Mater. Interfaces* **2017**, *9*, 17932.
- [35] Q.-B. Ma, B. Kaiser, J. Ziegler, D. Fertig, W. Jaegermann, *J. Phys. D. Appl. Phys.* **2012**, *45*, 325101.
- [36] Q. B. Ma, J. Ziegler, B. Kaiser, D. Fertig, W. Calvet, E. Murugasen, W. Jaegermann, *Int. J. Hydrogen Energy* **2014**, *39*, 1623.
- [37] M. Kato, T. Yasuda, K. Miyake, M. Ichimura, T. Hatayama, *Int. J. Hydrogen Energy* **2014**, *39*, 4845.
- [38] Q. Huang, Z. Ye, X. Xiao, *J. Mater. Chem. A* **2015**, *3*, 15824.
- [39] D. Kang, T. W. Kim, S. R. Kubota, A. C. Cardiel, H. G. Cha, K. S. Choi, *Chem. Rev.* **2015**, *115*, 12839.
- [40] P. Lianos, *Appl. Catal. B Environ.* **2017**, *210*, 235.
- [41] W. Yang, J. Moon, *ChemSusChem* **2019**, *11*, 1889.
- [42] J. Jian, G. Jiang, R. van de Krol, B. Wei, H. Wang, *Nano Energy* **2018**, *51*, 457.
- [43] S. Chu, W. Li, Y. Yan, T. Hamann, I. Shih, D. Wang, Z. Mi, *Nano Future* **2017**, *1*, 022001.
- [44] K. Rajeshwar, M. K. Hossain, R. T. Macaluso, C. Janáky, A. Varga, P. J. Kulesza, *J. Electrochem. Soc.* **2018**, *165*, H3192.
- [45] N. K. Awad, E. A. Ashour, N. K. Allam, *J. Renewable Sustainable Energy* **2014**, *6*, 022702.
- [46] I. Sullivan, B. Zoellner, P. A. Maggard, *Chem. Mater.* **2016**, *28*, 5999.
- [47] F. F. Abdi, S. P. Berglund, *J. Phys. D. Appl. Phys.* **2017**, *50*, 193002.
- [48] Y. J. Jang, J. S. Lee, *ChemSusChem* **2019**, *12*, 1835.
- [49] D. Monllor-Satoca, M. I. Díez-García, T. Lana-Villarreal, R. Gómez, *Chem. Commun.* **2020**, *56*, 12272.
- [50] J. H. Kim, H. E. Kim, J. H. Kim, J. S. Lee, *J. Mater. Chem. A* **2020**, *8*, 9447.
- [51] P. E. De Jongh, D. Vanmaekelbergh, J. J. Kelly, *J. Electrochem. Soc.* **2000**, *147*, 486.
- [52] C. A. N. Fernando, L. A. A. De Silva, R. M. Mehra, K. Takahashi, *Semicond. Sci. Technol.* **2001**, *16*, 433.
- [53] K. E. R. Brown, K. Choi, *Chem. Commun.* **2006**, 3311.
- [54] A. Paracchino, V. Laporte, K. Sivula, M. Grätzel, E. Thimsen, *Nat. Mater.* **2011**, *10*, 456.
- [55] Z. Zhang, P. Wang, *J. Mater. Chem.* **2012**, *22*, 2456.

- [56] Y.-K. Hsu, C.-H. Yu, H.-H. Lin, Y.-C. Chen, Y.-G. Lin, *J. Electroanal. Chem.* **2013**, *704*, 19.
- [57] P. Borno, F. F. Abdi, S. D. Tilley, B. Dam, R. Van De Krol, M. Graetzel, K. Sivula, *J. Phys. Chem. C* **2014**, *118*, 16959.
- [58] Y. Yang, D. Xu, Q. Wu, P. Diao, *Sci. Rep.* **2016**, *6*, 35158.
- [59] A. Paracchino, N. Mathews, T. Hisatomi, M. Stefiik, S. D. Tilley, M. Grätzel, *Energy Environ. Sci.* **2012**, *5*, 8673.
- [60] S. D. Tilley, M. Schreier, J. Azevedo, M. Stefiik, M. Grätzel, *Adv. Funct. Mater.* **2014**, *24*, 303.
- [61] M. Woodhouse, B. A. Parkinson, *Chem. Mater.* **2008**, *20*, 2495.
- [62] M. Woodhouse, B. A. Parkinson, *Chem Soc Rev* **2009**, *38*, 197.
- [63] K. Skorupska, B. A. Parkinson, in *Photoelectrochemical Solar Fuel Production: From Basic Principles To Advanced Devices* (Eds. S. Jiménez, J. Bisquet), Springer International Publishing, Switzerland, **2016**.
- [64] J. He, B. A. Parkinson, *ACS Comb. Sci.* **2011**, *13*, 399.
- [65] D. Seley, K. Ayers, B. A. Parkinson, *ACS Comb. Sci.* **2013**, *15*, 82.
- [66] C. Jiang, R. Wang, B. A. Parkinson, *ACS Comb. Sci.* **2013**, *15*, 639.
- [67] J. G. Rowley, T. D. Do, D. A. Cleary, B. A. Parkinson, *ACS Appl. Mater. Interfaces* **2014**, *6*, 9046.
- [68] P. F. Newhouse, B. A. Parkinson, *J. Mater. Chem. A* **2015**, *3*, 5901.
- [69] K. Skorupska, P. A. Maggard, R. Eichberger, K. Schwarzburg, P. Shahbazi, B. Zoellner, B. A. Parkinson, *ACS Comb. Sci.* **2015**, *17*, 742.
- [70] K. Sliozberg, H. S. Stein, C. Khare, B. A. Parkinson, A. Ludwig, W. Schuhmann, *ACS Appl. Mater. Interfaces* **2015**, *7*, 4883.
- [71] I. Kondofersky, A. Müller, H. K. Dunn, A. Ivanova, G. Štefanić, M. Ehrensperger, C. Scheu, B. A. Parkinson, D. Fattakhova-Rohlfing, T. Bein, *J. Am. Chem. Soc.* **2016**, *138*, 1860.
- [72] E. Casbeer, V. K. Sharma, X. Z. Li, *Sep. Purif. Technol.* **2012**, *87*, 1.
- [73] R. Dillert, D. H. Taffa, M. Wark, T. Bredow, D. W. Bahnemann, *APL Mater.* **2015**, *3*, 104001.
- [74] S. Saadi, A. Bouguelia, M. Trari, *Renewable Energy* **2006**, *31*, 2245.
- [75] H. Yang, J. Yan, Z. Lu, X. Cheng, Y. Tang, *J. Alloys Compd.* **2009**, *476*, 715.
- [76] G. Rekhila, Y. Bessekhoud, M. Trari, *Int. J. Hydrogen Energy* **2013**, *38*, 6335.
- [77] Y. Matsumoto, M. Omae, K. Sugiyama, E. Sato, *J. Phys. Chem.* **1987**, *91*, 577.
- [78] Y. Matsumoto, K. Sugiyama, E. Sato, *J. Electrochem. Soc.* **1988**, *135*, 98.
- [79] S. Ida, K. Yamada, T. Matsunaga, H. Hagiwara, Y. Matsumoto, T. Ishihara, *J. Am. Chem. Soc.* **2010**, *132*, 17343.
- [80] J. Cao, T. Kako, P. Li, S. Ouyang, J. Ye, *Electrochem. Commun.* **2011**, *13*, 275.
- [81] M. I. Díez-García, R. Gómez, *ACS Appl. Mater. Interfaces* **2016**, *8*, 21387.
- [82] K. Kirchberg, R. Marschall, *Sustainable Energy Fuels* **2019**, *3*, 1150.
- [83] N. Guijarro, P. Borno, M. Prévot, X. Yu, X. Zhu, M. Johnson, X. Jeanbourquin, F. Le Formal, K. Sivula, *Sustainable Energy Fuels* **2018**, *2*, 103.
- [84] X. Zhu, N. Guijarro, Y. Liu, P. Schouwink, R. A. Wells, F. Le Formal, S. Sun, C. Gao, K. Sivula, *Adv. Mater.* **2018**, *30*, 1801612.
- [85] Y. Liu, F. Le Formal, F. L. Yao, K. Sivula, N. Guijarro, *J. Mater. Chem. A* **2019**, *7*, 1669.
- [86] C. Lv, P. Liu, F. Huang, H. Zhang, X. Chu, S. Li, *J. Mater. Sci.* **2021**, *56*, 9408.
- [87] M. I. Díez-García, T. Lana-Villarreal, R. Gómez, *ChemSusChem* **2016**, *9*, 1504.
- [88] Y. Lan, Z. Liu, Z. Guo, M. Ruan, X. Li, *Chem. Commun.* **2020**, *56*, 5279.
- [89] S. Maitra, S. Pal, T. Maitra, S. Halder, S. Roy, *Energy and Fuels* **2021**, *35*, 14087.
- [90] T. Arai, Y. Konishi, Y. Iwasaki, H. Sugihara, K. Sayama, *J. Comb. Chem.* **2007**, *9*, 574.
- [91] N. T. Hahn, V. C. Holmberg, B. A. Korgel, C. B. Mullins, *J. Phys. Chem. C* **2012**, *116*, 6459.
- [92] R. Patil, S. Kelkar, R. Naphade, S. Ogale, *J. Mater. Chem. A* **2014**, *2*, 3661.
- [93] D. Kang, J. C. Hill, Y. Park, K.-S. Choi, *Chem. Mater.* **2016**, *28*, 4331.
- [94] S. P. Berglund, F. F. Abdi, P. Bogdanoff, A. Chemseddine, D. Friedrich, R. van de Krol, *Chem. Mater.* **2016**, *28*, 4231.
- [95] G. Sharma, Z. Zhao, P. Sarker, B. A. Nail, J. Wang, M. N. Huda, F. E. Osterloh, *J. Mater. Chem. A* **2016**, *4*, 2936.
- [96] D. Cao, N. Nasori, Z. Wang, Y. Mi, L. Wen, Y. Yang, S. Qu, Z. Wang, Y. Lei, *J. Mater. Chem. A* **2016**, *4*, 8995.
- [97] F. Wang, A. Chemseddine, F. F. Abdi, R. van de Krol, S. P. Berglund, *J. Mater. Chem. A* **2017**, *5*, 12838.
- [98] Y.-H. Choi, K. D. Yang, D.-H. Kim, K. T. Nam, S.-H. Hong, *Mater. Lett.* **2017**, *188*, 192.
- [99] I. Rodríguez-Gutiérrez, R. García-Rodríguez, M. Rodríguez-Pérez, A. Vega-Poot, G. Rodríguez Gattorno, B. A. Parkinson, G. Oskam, *J. Phys. Chem. C* **2018**, *122*, 27169.
- [100] J. Yang, C. Du, Y. Wen, Z. Zhang, K. Cho, R. Chen, B. Shan, *Int. J. Hydrogen Energy* **2018**, *43*, 9549.
- [101] J. Li, M. Griep, Y. Choi, D. Chu, *Chem. Commun.* **2018**, *54*, 3331.
- [102] F. E. Oropeza, B. T. Feleki, K. H. L. Zhang, E. J. M. Hensen, J. P. Hofmann, *ACS Appl. Energy Mater.* **2019**, *2*, 6866.
- [103] A. Song, P. Bogdanoff, A. Esau, I. Y. Ahmet, I. Levine, T. Dittrich, T. Unold, R. Van De Krol, S. P. Berglund, *ACS Appl. Mater. Interfaces* **2020**, *12*, 13959.
- [104] Y. Zhang, L. Wang, X. Xu, *Inorg. Chem. Front.* **2021**, *8*, 3863.
- [105] Z. Jiang, H. Geng, X. Cai, L. Mao, Y. Zhao, X. Gu, *Mater. Sci. Semicond. Process.* **2021**, *134*, 105989.
- [106] R. Gottesman, I. Levine, M. Schleunig, R. Irani, D. Abou-Ras, T. Dittrich, D. Friedrich, R. van de Krol, *Adv. Energy Mater.* **2021**, *11*, 2003474.
- [107] J. K. Cooper, Z. Zhang, S. Roychoudhury, C. M. Jiang, S. Gul, Y. S. Liu, R. Dhall, A. Ceballos, J. Yano, D. Prendergast, S. E. Reyes-Lillo, *Chem. Mater.* **2021**, *33*, 934.
- [108] G. Seo, B. Kim, S. W. Hwang, S. S. Shin, I. S. Cho, *Nano Energy* **2021**, *80*, 105568.
- [109] S. Kamimura, M. Higashi, R. Abe, T. Ohno, *J. Mater. Chem. A* **2016**, *4*, 6116.
- [110] H. Kawazoe, H. Yanagi, K. Ueda, H. Hosono, *MRS Bull.* **2000**, *25*, 28.
- [111] A. N. Banerjee, K. K. Chattopadhyay, *Prog. Cryst. Growth Charact. Mater.* **2005**, *50*, 52.
- [112] K. A. Vanaja, *PhD thesis*, Cochin University of Science and Technology, Cochin, Kerala (India), **2011**.
- [113] C. G. Read, Y. Park, K.-S. Choi, *J. Phys. Chem. Lett.* **2012**, *3*, 1872.
- [114] M. S. Prévot, N. Guijarro, K. Sivula, *ChemSusChem* **2015**, *8*, 1359.
- [115] M. S. Prévot, X. A. Jeanbourquin, W. S. Bourée, F. Abdi, D. Friedrich, R. van de Krol, N. Guijarro, F. Le Formal, K. Sivula, *Chem. Mater.* **2017**, *29*, 4952.
- [116] Y. Hermans, A. Klein, H. P. Sarker, M. N. Huda, H. Junge, T. Toupance, W. Jaegermann, *Adv. Funct. Mater.* **2020**, *30*, 1910432.
- [117] F. Boudoire, Y. Liu, F. Le Formal, N. Guijarro, C. R. Lhermitte, K. Sivula, *J. Phys. Chem. C* **2021**, *125*, 10883.
- [118] Y. Oh, W. Yang, J. Kim, S. Jeong, J. Moon, *ACS Appl. Mater. Interfaces* **2017**, *9*, 14078.
- [119] Y. Oh, W. Yang, J. Tan, H. Lee, J. Park, J. Moon, *Nanoscale* **2018**, *10*, 3720.
- [120] T. Jiang, Y. Zhao, M. Liu, Y. Chen, Z. Xia, H. Xue, *Phys. Status Solidi A* **2018**, *215*, 1800056.

- [121] Y. Oh, W. Yang, J. Tan, H. Lee, J. Park, J. Moon, *Adv. Funct. Mater.* **2019**, *29*, 1900194.
- [122] I. Garcia-Torregrosa, Y. G. Geertzema, A. S. M. Ismail, T. L. Lee, F. M. F. de Groot, B. M. Weckhuysen, *ChemPhotoChem* **2019**, *3*, 1238.
- [123] C. M. Jiang, S. E. Reyes-Lillo, Y. Liang, Y. S. Liu, G. Liu, F. M. Toma, D. Prendergast, I. D. Sharp, J. K. Cooper, *Chem. Mater.* **2019**, *31*, 2524.
- [124] M. Ferri, J. D. Elliott, M. F. Camellone, S. Fabris, S. Piccinin, *ACS Catal.* **2021**, *11*, 1897.
- [125] M. Ferri, J. Elliott, M. Farnesi Camellone, S. Fabris, S. Piccinin, *J. Phys. Chem. C* **2019**, *123*, 29589.
- [126] J. Gu, Y. Yan, J. W. Krizan, Q. D. Gibson, Z. M. Detweiler, R. J. Cava, A. B. Bocarsly, *J. Am. Chem. Soc.* **2014**, *136*, 830.
- [127] J. E. Park, Y. Hu, J. W. Krizan, Q. D. Gibson, U. T. Tayvah, A. Selloni, R. J. Cava, A. B. Bocarsly, *Chem. Mater.* **2018**, *30*, 2574.
- [128] M. Lee, D. Kim, Y. T. Yoon, Y. Il Kim, *Bull. Korean Chem. Soc.* **2014**, *35*, 3261.
- [129] A. K. Díaz-García, T. Lana-Villarreal, R. Gómez, *J. Mater. Chem. A* **2015**, *3*, 19683.
- [130] M. Levy, *PhD thesis*, Imperial College London, London, UK, **2005**.
- [131] T. Ishihara, in *Perovskite Oxide Solid Oxide Fuel Cells* (Ed.: T. Ishihara), Springer Science+Business Media, LLC, New York, NY, USA **2009**.
- [132] S. Mitra, *Developments in Geochemistry 9. High-Pressure Geochemistry and Mineral Physics. Basics for Planetology and Geo-Material Science*, Elsevier B.V., Amsterdam, The Netherlands, **2004**.
- [133] P. Company, *Surf. Sci.* **1980**, *101*, 205.
- [134] H. S. Jarrett, A. W. Sleight, H. H. Kung, J. L. Gillson, *J. Appl. Phys.* **1980**, *51*, 3916.
- [135] S. Joiret, G. Campet, J. Claverie, *Mater. Lett.* **1987**, *5*, 468.
- [136] U. A. Joshi, A. M. Palasyuk, P. A. Maggard, *J. Phys. Chem. C* **2011**, *115*, 13534.
- [137] V. Celorrio, K. Bradley, O. J. Weber, S. R. Hall, D. J. Fermín, *ChemElectroChem* **2014**, *1*, 1667.
- [138] Q. Yu, X. Meng, T. Wang, P. Li, L. Liu, K. Chang, G. Liu, J. Ye, *Chem. Commun.* **2015**, *51*, 3630.
- [139] M. I. Díez-García, R. Gómez, *ChemSusChem* **2017**, *10*, 2457.
- [140] G. S. Pawar, A. A. Tahir, *Sci. Rep.* **2018**, *8*, 3501.
- [141] M. K. Son, H. Seo, M. Watanabe, M. Shiratani, T. Ishihara, *Nanoscale* **2020**, *12*, 9653.
- [142] J. Quiñonero, F. J. Pastor, J. M. Orts, R. Gómez, *ACS Appl. Mater. Interfaces* **2021**, *13*, 14150.
- [143] E. Freeman, S. Kumar, S. R. Thomas, H. Pickering, D. J. Fermin, S. Eslava, *ChemElectroChem* **2020**, *7*, 1365.
- [144] G. P. Wheeler, K.-S. Choi, *ACS Energy Lett.* **2017**, *2*, 2378.
- [145] E. Freeman, S. Kumar, V. Celorrio, M. S. Park, J. H. Kim, D. J. Fermin, S. Eslava, *Sustainable Energy Fuels* **2020**, *4*, 884.
- [146] M. I. Díez-García, V. Celorrio, L. Calvillo, D. Tiwari, R. Gómez, D. J. Fermín, *Electrochim. Acta* **2017**, *246*, 365.
- [147] I. N. Sora, F. Fontana, R. Passalacqua, C. Ampelli, S. Perathoner, G. Centi, F. Parrino, L. Palmisano, *Electrochim. Acta* **2013**, *109*, 710.
- [148] Q. Peng, B. Shan, Y. Wen, R. Chen, *Int. J. Hydrogen Energy* **2015**, *40*, 15423.
- [149] Q. Peng, Y. Wen, B. Shan, R. Chen, *ECS Trans.* **2015**, *64*, 27.
- [150] Q. Peng, J. Wang, Y. W. Wen, B. Shan, R. Chen, *RSC Adv.* **2016**, *6*, 26192.
- [151] Y. Guo, N. Zhang, H. Huang, Z. Li, Z. Zou, *RSC Adv.* **2017**, *7*, 18418.
- [152] I. M. Nassar, S. Wu, L. Li, X. Li, *ChemistrySelect* **2018**, *3*, 968.
- [153] Y. Liu, J. Quiñonero, L. Yao, X. Da Costa, M. Mensi, R. Gómez, K. Sivula, N. Guijarro, *J. Mater. Chem. A* **2021**, *9*, 2888.
- [154] W. Ji, K. Yao, Y. F. Lim, Y. C. Liang, A. Suwardi, *Appl. Phys. Lett.* **2013**, *103*, 062901.
- [155] L. T. Quynh, C. N. Van, Y. Bitla, J. W. Chen, T. H. Do, W. Y. Tzeng, S. C. Liao, K. A. Tsai, Y. C. Chen, C. L. Wu, C. H. Lai, C. W. Luo, Y. J. Hsu, Y. H. Chu, *Adv. Energy Mater.* **2016**, *6*, 1600686.
- [156] T. Yu, F. Gao, H. T. Zhang, L. F. Liu, Y. M. Wang, Z. S. Li, Z. G. Zou, J. M. Liu, *Appl. Phys. Lett.* **2007**, *91*, 022114.
- [157] Q. Liu, Y. Zhou, L. You, J. Wang, M. Shen, L. Fang, *Appl. Phys. Lett.* **2016**, *108*, 022902.
- [158] P. Yilmaz, D. Yeo, H. Chang, L. Loh, S. Dunn, *Nanotechnology* **2016**, *27*, 345402.
- [159] Y. Ren, F. Nan, L. You, Y. Zhou, Y. Wang, J. Wang, X. Su, M. Shen, L. Fang, *Small* **2017**, *13*, 1603457.
- [160] S. Gu, X. Zhou, F. Zheng, L. Fang, W. Dong, M. Shen, *Chem. Commun.* **2017**, *53*, 7052.
- [161] H. Shen, X. Zhou, W. Dong, X. Su, L. Fang, X. Wu, M. Shen, *Appl. Phys. Lett.* **2017**, *111*, 123901.
- [162] J. Ge, W.-J. Yin, Y. Yan, *Chem. Mater.* **2018**, *30*, 1017.
- [163] L. Fuoco, U. A. Joshi, P. A. Maggard, *J. Phys. Chem. C* **2012**, *116*, 10490.
- [164] I. Sullivan, P. P. Sahoo, L. Fuoco, A. S. Hewitt, S. Stuart, D. Dougherty, P. A. Maggard, *Chem. Mater.* **2014**, *26*, 6711.
- [165] U. A. Joshi, P. A. Maggard, *J. Phys. Chem. Lett.* **2012**, *3*, 1577.
- [166] A. Kormányos, A. Thomas, M. N. Huda, P. Sarker, J. P. Liu, N. Poudyal, C. Janáky, K. Rajeshwar, *J. Phys. Chem. C* **2016**, *120*, 16024.
- [167] J. Choi, N. King, P. A. Maggard, *ACS Nano* **2013**, *7*, 1699.
- [168] S. Kamimura, N. Murakami, T. Tsubota, T. Ohno, *Appl. Catal. B Environ.* **2015**, *174–175*, 471.
- [169] P. P. Sahoo, B. Zoellner, P. A. Maggard, *J. Mater. Chem. A* **2015**, *3*, 4501.
- [170] A. Song, S. P. Berglund, A. Chemseddine, D. Friedrich, F. F. Abdi, R. Van De Krol, *J. Mater. Chem. A* **2020**, *8*, 12538.
- [171] G. P. Wheeler, K.-S. Choi, *ACS Appl. Energy Mater.* **2018**, *1*, 4917.
- [172] J. Tian, Q. Liu, Y. Liang, Z. Xing, A. M. Asiri, X. Sun, *ACS Appl. Mater. Interfaces* **2014**, *6*, 20579.
- [173] S. Chen, S. S. Thind, A. Chen, *Electrochem. Commun.* **2016**, *63*, 10.
- [174] X. Chen, C. Burda, *J. Am. Chem. Soc.* **2008**, *130*, 5018.
- [175] X. Chen, S. S. Mao, *Chem. Rev.* **2007**, *107*, 2891.
- [176] S. Zhang, H. Ye, J. Hua, H. Tian, *EnergyChem* **2019**, *1*, 100015.
- [177] K. Iwashina, A. Kudo, *J. Am. Chem. Soc.* **2011**, *133*, 13272.
- [178] S. Kawasaki, K. Nakatsuji, J. Yoshinobu, F. Komori, R. Takahashi, M. Lippmaa, K. Mase, A. Kudo, *Appl. Phys. Lett.* **2012**, *101*, 033910.
- [179] G. P. Wheeler, V. U. Baltazar, T. J. Smart, A. Radmilovic, Y. Ping, K. S. Choi, *Chem. Mater.* **2019**, *31*, 5890.
- [180] Y. Li, T. Wang, B. Gao, X. Fan, H. Gong, H. Xue, S. Zhang, X. Huang, J. He, *New J. Chem.* **2021**, *45*, 3463.
- [181] B. Zoellner, S. Stuart, C.-C. Chung, D. B. Dougherty, J. L. Jones, P. A. Maggard, *J. Mater. Chem. A* **2016**, *4*, 3115.
- [182] H. Kumagai, G. Sahara, K. Maeda, M. Higashi, R. Abe, O. Ishitani, *Chem. Sci.* **2017**, *8*, 4242.
- [183] C. E. Creissen, J. Warnan, E. Reisner, *Chem. Sci.* **2018**, *9*, 1439.
- [184] F. Li, R. Xu, C. Nie, X. Wu, P. Zhang, L. Duan, L. Sun, *Chem. Commun.* **2019**, *55*, 12940.
- [185] X. Li, A. Liu, D. Chu, C. Zhang, Y. Du, J. Huang, P. Yang, *Catalysts* **2018**, *8*, 108.
- [186] X. Chen, J. Ye, S. Ouyang, T. Kako, Z. Li, Z. Zou, *ACS Nano* **2011**, *5*, 4310.
- [187] X. Shi, K. Zhang, K. Shin, J. H. Moon, T.-W. Lee, J. H. Park, *Phys. Chem. Chem. Phys.* **2013**, *15*, 11717.
- [188] M. Zhou, J. Bao, Y. Xu, J. Zhang, J. Xie, M. Guan, C. Wang, L. Wen, Y. Lei, Y. Xie, *ACS Nano* **2014**, *8*, 7088.
- [189] V. Hasija, A. Kumar, A. Sudhaik, P. Raizada, P. Singh, Q. Van Le, T. T. Le, V. H. Nguyen, *Environ. Chem. Lett.* **2021**, *19*, 2941.

- [190] E. S. Kim, H. J. Kang, G. Magesh, J. Y. Kim, J. Jang, J. S. Lee, *ACS Appl. Mater. Interfaces* **2014**, *6*, 17762.
- [191] N. Srinivasan, E. Sakai, M. Miyauchi, *ACS Catal.* **2016**, *6*, 2197.
- [192] M. G. Ahmed, T. A. Kandiell, A. Y. Ahmed, I. Kretschmer, F. A. Rashwan, D. W. Bahnmann, *J. Phys. Chem. C* **2015**, *119*, 5864.
- [193] E. S. Kim, N. Nishimura, G. Magesh, J. Y. Kim, J. Jang, H. Jun, J. Kubota, K. Domen, J. S. Lee, *J. Am. Chem. Soc.* **2013**, *135*, 5375.
- [194] Y. Liu, H. He, J. Li, W. Li, Y. H. Yang, Y. Li, Q. Chen, *RSC Adv.* **2015**, *5*, 99378.
- [195] X. Long, C. Wang, S. Wei, T. Wang, J. Jin, J. Ma, *ACS Appl. Mater. Interfaces* **2020**, *12*, 2452.
- [196] X. Long, T. Wang, J. Jin, X. Zhao, J. Ma, *Nanoscale* **2021**, *13*, 11215.
- [197] R. Liu, Z. Zheng, J. Spurgeon, X. Yang, *Energy Environ. Sci.* **2014**, *7*, 2504.
- [198] J. Azevedo, L. Steier, P. Dias, M. Stefik, C. T. Sousa, J. P. Araújo, A. Mendes, M. Graetzel, S. D. Tilley, *Energy Environ. Sci.* **2014**, *7*, 4044.
- [199] A. K. Shah, T. K. Sahu, A. Banik, D. Gogoi, N. R. Peela, M. Qureshi, *Sustainable Energy Fuels* **2019**, *3*, 1554.
- [200] J. Lee, H. Yoon, S. Kim, S. Seo, J. Song, B. U. Choi, S. Y. Choi, H. Park, S. Ryu, J. Oh, S. Lee, *Chem. Commun.* **2019**, 55, 12447.
- [201] Z. Zhang, S. A. Lindley, D. Guevarra, K. Kan, A. Shinde, J. M. Gregoire, W. Han, E. Xie, J. A. Haber, J. K. Cooper, *Adv. Funct. Mater.* **2020**, *30*, 2000948.
- [202] Q. Zhang, B. Zhai, Z. Lin, X. Zhao, P. Diao, *J. Phys. Chem. C* **2021**, *125*, 1890.
- [203] A. Song, I. Levine, R. Van De Krol, T. Dittrich, S. P. Berglund, *Chem. Sci.* **2020**, *11*, 11195.
- [204] X. Yan, R. Pu, R. Xie, B. Zhang, Y. Shi, W. Liu, G. Ma, N. Yang, *Appl. Surf. Sci.* **2021**, 552, 149442.
- [205] N. Xu, F. Li, L. Gao, H. Hu, Y. Hu, X. Long, J. Ma, J. Jin, *Int. J. Hydrogen Energy* **2018**, *43*, 2064.
- [206] M. S. Prévot, Y. Li, N. Guijarro, K. Sivula, *J. Mater. Chem. A* **2016**, *4*, 3018.
- [207] A. Song, P. Plate, A. Chemseddine, F. Wang, F. F. Abdi, M. Wollgarten, R. Van De Krol, S. P. Berglund, *J. Mater. Chem. A* **2019**, *7*, 9183.
- [208] H. S. Park, C.-Y. Lee, E. Reisner, *Phys. Chem. Chem. Phys.* **2014**, *16*, 22462.
- [209] M. K. Hossain, G. F. Samu, K. Gandha, S. Santhanagopalan, J. P. Liu, C. Janáky, K. Rajeshwar, *J. Phys. Chem. C* **2017**, *121*, 8252.
- [210] S. A. Monny, L. Zhang, Z. Wang, B. Luo, M. Konarova, A. Du, L. Wang, *J. Mater. Chem. A* **2020**, *8*, 2498.
- [211] Q. Zhang, B. Zhai, Z. Lin, X. Zhao, P. Diao, *Int. J. Hydrogen Energy* **2021**, *46*, 11607.
- [212] Y. Matsumoto, K. Sugiyama, E.-I. Sato, *J. Solid State Chem.* **1988**, *74*, 117.
- [213] X. Sun, D. Tiwari, D. J. Fermin, *ACS Appl. Mater. Interfaces* **2020**, *12*, 31486.
- [214] Q. Deng, H. Chen, G. Wang, Y. Shen, F. Liu, S. Wang, *Ceram. Int.* **2020**, *46*, 598.
- [215] K. Sekizawa, T. Nonaka, T. Arai, T. Morikawa, *ACS Appl. Mater. Interfaces* **2014**, *6*, 10969.
- [216] Y. J. Jang, Y. Bin Park, H. E. Kim, Y. H. Choi, S. H. Choi, J. S. Lee, *Chem. Mater.* **2016**, *28*, 6054.
- [217] S. Park, J. H. Baek, L. Zhang, J. M. Lee, K. H. Stone, I. S. Cho, J. Guo, H. S. Jung, X. Zheng, *ACS Sustainable Chem. Eng.* **2019**, *7*, 5867.
- [218] T. Berger, T. Lana-Villarreal, D. Monllor-Satoca, R. Gómez, *Electrochem. Commun.* **2006**, *8*, 1713.
- [219] M. I. Díez-García, D. Monllor-Satoca, V. Vinoth, S. Anandan, T. Lana-Villarreal, *ChemElectroChem* **2017**, *4*, 1429.
- [220] F. Wang, W. Septina, A. Chemseddine, F. F. Abdi, D. Friedrich, P. Bogdanoff, R. van de Krol, S. D. Tilley, S. P. Berglund, *J. Am. Chem. Soc.* **2017**, *139*, 15094.
- [221] J. Yang, D. Wang, H. Han, C. Li, *Acc. Chem. Res.* **2013**, *46*, 1900.
- [222] P. Chatchai, A. Y. Nosaka, Y. Nosaka, *Electrochemistry* **2011**, *79*, 821.
- [223] Z. Jin, Z. Hu, J. C. Yu, J. Wang, *J. Mater. Chem. A* **2016**, *4*, 13736.
- [224] Y. Lin, C. Battaglia, M. Boccard, M. Hettick, Z. Yu, C. Ballif, J. W. Ager, A. Javey, *Nano Lett.* **2013**, *13*, 5615.
- [225] N. P. Dasgupta, C. Liu, S. Andrews, F. B. Prinz, P. Yang, *J. Am. Chem. Soc.* **2013**, *135*, 12932.
- [226] X. Sun, D. Tiwari, D. J. Fermin, *J. Electrochem. Soc.* **2019**, *166*, H764.
- [227] S. Somasundaram, C. Raman Nair Chenthamarakshan, N. R. de Tacconi, K. Rajeshwar, *Int. J. Hydrogen Energy* **2007**, *32*, 4661.
- [228] A. A. Dubale, C.-J. Pan, A. G. Tamirat, H.-M. Chen, W.-N. Su, C.-H. Chen, J. Rick, D. W. Ayele, B. A. Aragaw, J.-F. Lee, Y.-W. Yang, B.-J. Hwang, *J. Mater. Chem. A* **2015**, *3*, 12482.
- [229] F. N. I. Sari, C. Lin, J.-M. Ting, *Chem. Eng. J.* **2019**, *368*, 784.
- [230] C. G. Morales-Guio, L. Liardet, M. T. Mayer, S. D. Tilley, M. Grätzel, X. Hu, *Angew. Chem. Int. Ed.* **2015**, *54*, 664.
- [231] C.-Y. Lin, Y.-H. Lai, D. Mersch, E. Reisner, *Chem. Sci.* **2012**, *3*, 3482.
- [232] M. Shao, R. Zhang, Z. Li, M. Wei, D. G. Evans, X. Duan, *Chem. Commun.* **2015**, 51, 15880.
- [233] Y. Nakabayashi, M. Nishikawa, Y. Nosaka, *Electrochim. Acta* **2014**, *125*, 191.
- [234] O. Palasyuk, A. Palasyuk, P. A. Maggard, *J. Solid State Chem.* **2010**, *183*, 814.
- [235] D. T. Sawyer, A. Sobkowiak, J. L. Roberts, *Electrochemistry For Chemists*, John Wiley & Sons, New York, NY, USA **1995**.



**María Isabel Díez-García** obtained her B.Sc. in chemical engineering and her M.Sc. in material science at University of Alicante. In 2018, she obtained her Ph.D. for the study of metal oxide photocathodes for hydrogen production under the supervision of Prof. R. Gómez in the same university, and later she continued as a postdoctoral researcher at the same group, working on solar energy conversion. Most recently, she joined the Catalonia Institute for Energy Research (IREC) as a Juan de la Cierva postdoctoral fellow with Prof. J. R. Morante. Among her research interests are the fundamentals and applications of (photo)electrochemistry for energy conversion.



**Roberto Gómez** obtained his Ph.D. in chemistry from the University of Alicante in 1994. Subsequently, he was postdoctoral researcher at Purdue University, his work focusing on the application of vibrational spectroscopies to the electrode/solution interface. He returned to the University of Alicante, where he is currently professor and head of the Department of Physical Chemistry. After stays at the University of Bath (under Prof. L.M. Peter) and the National Renewable Energy Laboratory (under Dr. A.J. Nozik), he became interested in the electrochemistry of semiconductors and, more particularly, in photoelectrochemistry for the conversion of solar energy into electrical or chemical energy.